Chapter 4: Optical Characterisation

Chapter 2 discusses the growth and etching. Chapter 3 is a discussion of the

mechanical characterisation of the ZTS crystal. ZTS being a nonlinear optical crystal,

growth technique adopted should yield a crystal with suitable optical properties in

addition to its mechanical robustness. In this chapter, we discuss, work undertaken to

characterise both the linear and nonlinear optical properties of ZTS is discussed in this

chapter. This chapter is divided into two parts. Part A describes second harmonic

generation and laser damage studies on ZTS crystals. Part B deals with other optical

characterisation. In particular this part deals with absorption studies, which involve

traditional transmission measurements as well as thermal lensing and Z-scan techniques

to characterise the very small absorption and the thermo-optical coefficients of the ZTS

crystals.

PART A: Second Harmonic Generation and Laser Damage

4.1. Second Harmonic Generation

4.1.1. Introduction

Non-linear optics (NLO) deals the modification of material properties by electromagnetic radiation. A concise synopsis of the subject was first published in 1962 by Armstrong *et al.*, in which the basic concept of the non-linear susceptibility of a material media was first understood in terms of Maxwell equations and quantum mechanics.[1] Although many interesting phenomena arise from non-linear interactions, we will primarily focus on the scenario in which two photons at frequency ω are annihilated simultaneously creating a new photon of frequency 2ω. This simplest and best-known example of a non-linear process is commonly referred to as frequency doubling, or second harmonic generation (SHG).

Generation of laser light at any given wavelength is often either impossible due to non-availability of appropriate laser gain materials or inconvenient due to bulky laser systems. In many cases, the required wavelengths can be generated by frequency mixing processes such as Second Harmonic Generation (SHG). SHG is the process of generating a laser beam at a required wavelength from another laser source with twice the required wavelength. Over the last few years several applications require compact laser sources at visible and near ultraviolet (UV) wavelengths. With the availability of high-power solid-state laser sources at near infrared (NIR) wavelengths, the generation of blue and near UV via second harmonic process.

Currently, Gallium Nitride-based blue laser diodes at specific wavelengths are becoming available in the market.[2] However, their low output power limits their domain of application and hence, SHG-based laser sources continue to be a viable technology.[3,4] Several inorganic crystals such as potassium titanyl phosphate (KTiOPO$_4$ or KTP),[5] lithium niobate (LiNbO$_3$)[6] and beta barium borate (BBO)[7] have been used for SHG applications. These materials coupled with availability of several NIR laser sources constitute viable options for generation of coherent blue and near-UV light that can be utilised for numerous applications. These applications include high-density optical data storage,[8] printing,[9] spectroscopy,[10,11] inspection, biomedicine[12] and others.[13,14,15]

All dielectric materials become non-linear when subjected to intense electromagnetic fields. An induced net dipole moment or polarisation is created when an incident sinusoidal field in time displaces both electrons and nuclei from their equilibrium positions in a localised region. Following similar treatment by Boyd,[16] the macroscopic polarisation induced by the fundamental field can be expressed by

$$P_i = \varepsilon_0 \left(\chi_{ij}^{(1)} E_j + \chi_{ijk}^{(2)} E_j E_k + \chi_{ijkl}^{(3)} E_j E_k E_l + \ldots\ldots \right), \qquad (4.1.1)$$

where ε_0 is the permitivity of free space, $\chi^{(n)}$ is the susceptibility tensor of rank (n+1) which involves n different frequencies, and each index j, k, l represents the Cartesian components, x, y, z of the incident electric E-fields. The first order term, $\chi^{(1)}$, is the linear susceptibility. It gives rise to dispersion, refraction and reflection. In the case for which this term dominates, a material's linear nature dictates a harmonic potential where the induced dipole moment responds to a linear restoring force. The second order term, $\chi^{(2)}$, is the lowest order non-linear susceptibility term responsible for the second harmonic generation,[17] sum and difference frequency mixing,[18] parametric oscillation,[19] and the

linear electro-optics or Pockles effect.[20] This term vanishes in materials possessing inversion symmetry, which can be destroyed by an applied electrostatic field or due to the spatial inhomogeneous characteristic of an anisotropic medium. A high $\chi^{(2)}$ value in non-centrosymmetric materials such as KTP and LiNbO$_3$, represents a nonlinear anharmonic potential response. The third order term, $\chi^{(3)}$, gives rise to third harmonic generation,[21] the quadratic electro-optic or Kerr effect,[22] two photon absorption,[23] and Raman,[24] Brillouin,[25] and Rayleigh scattering.[26]

Due to the frequency dependence of the properties of the material, it is convenient to make a Fourier decomposition of both $P_i^{(n)}$ and E_i in equation (4.1.1) and to relate the Fourier components $P_i^{(n)}(\omega)$ and $E_i(\omega)$ by a power series.[27] For SHG, the tensor property of $\chi^{(2)}$ is displayed in the second–order polarisation[28]

$$P_i^{(2)}(2\omega) = \varepsilon_o \sum \chi_{ijk}^{(2)}(-2\omega,\omega,\omega)E_j(\omega)E_k(\omega)$$
$$P_i^{(2)}(2\omega) = \varepsilon_o \sum 2d_{ijk}(-2\omega,\omega,\omega)E_j(\omega)E_k(\omega)$$

(4.1.2)

which expresses a quadratic non-linearity that describes a three-wave mixing process where two E-fields of fundamental frequency ω interact and generate a third field at 2ω. This process can be readily understood when the product of the two fields sinusoidal in time is taken

$$\sin^2(\omega t) = \frac{1}{2}[1 - \cos(2\omega t)],$$

(4.1.3)

which is equivalent to a cosine term with twice the fundamental frequency.

One material property that plays a dominant role in the efficiency of the frequency conversion process is optical dispersion. In an anisotropic medium, a monochromatic field $E(\omega)$ at frequency ω will propagate with phase velocity

corresponding to the index of refraction, n_ω, and generate the polarisation wave $P(2\omega)$ with the same phase velocity as the incident field. The second order polarisation acts as a source of an electric field $E(2\omega)$ which propagates at a phase velocity corresponding to $n_{2\omega}$. In most materials the presence of normal dispersion of a media means that $n_{2\omega} > n_\omega$ and this results of the second harmonic generation periodic generation and extinction. This is illustrated in the figure 4.1.1. Curve (a) shows the oscillation of the fundamental field $E(\omega)$ in time. Curve (b) shows the oscillation of the resulting second order non-linear polarisation wave $P(2\omega)$ proportional to $E^2(2\omega)$. The two curves (c) and (d) show the oscillation of the second harmonic wave at the input end $(z = 0)$ and at any point further into the crystal $(z = l)$. These two oscillations periodically fall in an out of step along the propagation direction z owing to different velocities corresponding to n_ω and $n_{2\omega}$. This results in the generation and extinction of the second harmonic output periodically over a characteristic distance called the coherence length l_c. Phase-matching is a process by which the coherence length l_c can be made arbitrarily large to ensure build up of the second harmonic output over the entire length of the crystal. Phase-matching is discussed in detail in the following sections.
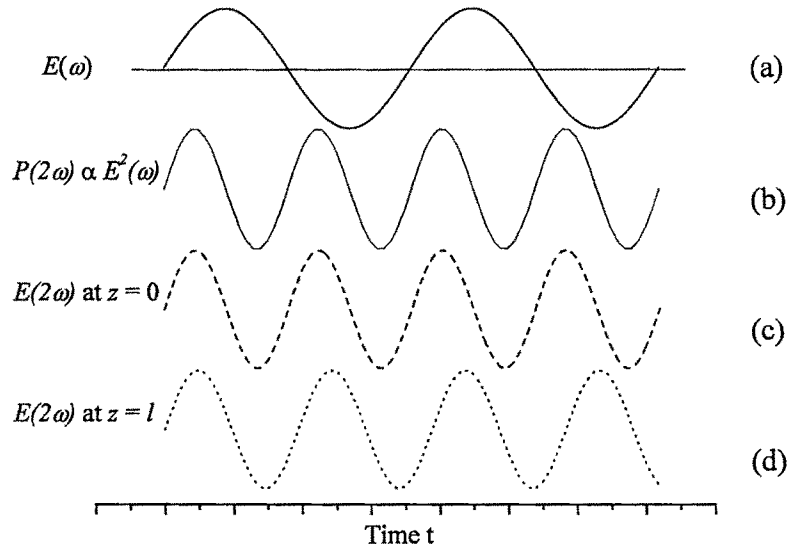
$E(\omega)$ (a)

$P(2\omega) \propto E^2(\omega)$ (b)

$E(2\omega)$ at $z = 0$ (c)

$E(2\omega)$ at $z = l$ (d)

Time t

Figure 4.1.1 The second harmonic output undergoes periodic generation and extinction. The top curve (a) shows the oscillation of the fundamental field $E(\omega)$ in time. The curve (b) shows the oscillation of the resulting second order non-linear polarisation wave. The two curves (c) and (d) show the oscillation of the second harmonic wave at the input end ($z = 0$) and at any point further into the crystal ($z = l$). These two oscillations periodically fall in an out of step along the propagation direction since the second harmonic wave travels at a different velocity than the fundamental wave. This results in the periodic generation and extinction of the second harmonic output.

4.1.2. Phase Matching

Conversation of energy $(\omega + \omega = 2\omega)$ and conservation of momentum $(2k_\omega = k_\omega)$ are conditions required for efficient seconds harmonic generation. The second condition, also referred to as the phase-matching condition, can be achieved by matching the refractive indices at the fundamental and the second harmonic wavelengths as expressed by

$$n(\omega) = n(2\omega) \qquad (4.1.4)$$

At first glance, it seems almost impossible to satisfy the second condition in dispersive media by matching the refractive indices.

However a practical technique for satisfying the phase-matching condition was first suggested by Giordmaine et al.[29] and independently by Maker et al.[30] They showed that it is possible to achieve phase matching by utilising the natural birefringence of the anisotropic crystal to offset dispersion. In general, anisotropic media in which second-order non-linear processes are possible exhibit the phenomenon of birefringence. In such media, the index of refraction (and thus the phase velocity) for a wave at a given frequency depends on its state of polarisation as well as the direction of propagation in the crystal. A detailled discussion of phase matching for second harmonic generation can be found in Ref. 31. It is shown that for an arbitrary propagation direction in a birefringent crystal, two orthogonal linear polarisation states are permitted.[32] This effect is called double refraction (walk off). The anisotropic medium is called a uniaxial crystal if the refractive index (and phase velocity) for one of these polarisation states is constant and independent of the direction of propagation. If the refractive indices of both

polarisation states vary with direction of propagation, the anisotropic medium is referred to as a biaxial crystal. Crystals with trigonal, tetragonal and hexagonal symmetries are always uniaxial (e.g. ADP, KDP) and crystals with orthorhombic, monoclinic, and triclinic symmetries are always biaxial (e.g. KTP, BTCC). To determine the orientation and phase velocities of the two allowed polarisation vectors in a given direction, it is often convenient to use the so-called optical indicatrix. An excellent discussion of the optical indicatrix can be found in Ref. 33.

➤ **The Optical Indicatrix:**

In an anisotropic medium, the change in the refractive indices with the direction of light propagation is represented by a three-dimensional geometric figure known as the optical indicatrix, which has three planes of symmetry. The optical indicatrix is a construction whose axes are in the direction of the principal optical axes (*x, y, z*) of the birefringent crystal. The magnitudes of the semi-axes are equal to the principal indices of refraction, n_x, n_y, and n_z. n_x, n_y and n_z are the refractive indices for waves *polarised in* the *x, y* and *z* directions, respectively. By convention we set $n_x \leq n_y \leq n_z$.[34, 35]

We first begin the discussion of birefringence in a uniaxial crystal and will then extend it to biaxial crystals. A light wave entering a uniaxial crystal is polarised into two mutually perpendicular directions. For one of these polarisations the refractive index does not vary with the direction of propagation of the wave. This wave is called the ordinary wave (o-wave). The wave with the orthogonal polarisation is referred to as the extraordinary wave (e-wave). In uniaxial crystals, there exists a unique direction of propagation along which the refractive indices for both the ordinary and the extraordinary

waves are equal. This direction is called the *optic axis* of the uniaxial crystal. The plane containing the direction of propagation and the optic axis is called an *optic plane*. If the refractive index for the extraordinary wave (n_e) is always less than or equal to that for the ordinary wave (n_o) the crystal is referred to as a negative uniaxial crystal. For a positive uniaxial crystal $n_e \geq n_o$.

Figure 4.1.2, shows a schematic diagram the variation of refractive index with direction of propagation for a negative uniaxial crystal at both the fundamental (ω) and the second harmonic frequencies (2ω).[31] Due to normal dispersion, the refractive index in most crystals in the visible and near infrared spectrum decreases with wavelength. Therefore for the same polarisation the refractive index at the second harmonic wavelength is larger than that at the fundamental wavelength. The circles represent the polar plots of the refractive index for the ordinary waves, n_o^{ω} and $n_o^{2\omega}$, at ω and 2ω, respectively, as a function of propagation direction. The ellipses represent the refractive indices $n_e^{\omega}(\phi)$ and $n_e^{2\omega}(\phi)$ for the extraordinary waves. At a fixed wavelength, the refractive index as a function of the propagation direction (ϕ) for the extraordinary wave is given by the equation of an ellipse,

$$\frac{1}{n_e^2(\phi)} = \frac{\cos^2\phi}{n_z^2} + \frac{\sin^2\phi}{n_x^2} \qquad (4.1.5)$$

where n_x and n_z are the refractive indices along the x- and the z-axis, respectively. For the negative uniaxial crystals n_z would correspond to the ordinary refractive index, n_o. As expected, the smaller circle (n_o^{ω}) and the smaller ellipse [$n_e^{\omega}(\phi)$] are for the fundamental wavelengths. The phase-matching directions are given by the intersection of the
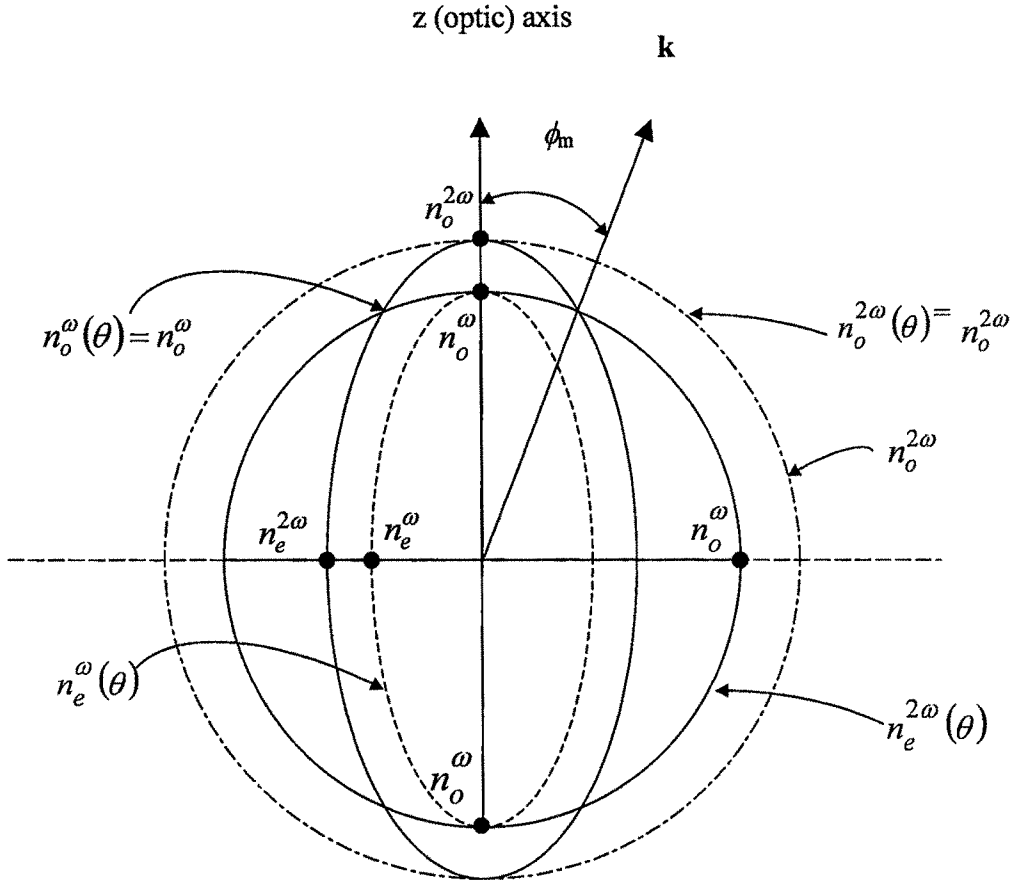
112

z (optic) axis

k

Figure 4.1.2. Phase matching in a negative uniaxial crystal: The figure shows a schematic polar plot of the variation of refractive index with propagation direction for a uniaxial crystal. The circles represent the refractive indices n_0^ω and $n_0^{2\omega}$ of the ordinary waves at the fundamental (ω) and second harmonic (2ω) frequencies, respectively. The ellipses represent the extraordinary refractive indices $n_e^\omega(\phi)$ and $n_e^{2\omega}(\phi)$ at ω and 2ω, respectively. At the phase matching direction k, indicated by the phase matching angle ϕ_m, the extraordinary refractive index at 2ω equals the ordinary refractive index at ω.. Or in other words $n_e^{2\omega}(\phi_m) = n_0^\omega$. From Ref.31

fundamental circle (n_0^ω) and the second harmonic ellipse [$n_e^{2\omega}(\phi)$]. At these directions (ϕ) the phase-matching condition, $n_0^\omega = n_e^{2\omega}(\phi)$, is satisfied.

The determination of the phase-matching directions in a biaxial crystal is somewhat a complex process. The difficulty arises from the fact that in a biaxial crystal the refractive indices of not one, but both allowed polarisation may vary with the direction of propagation, so one cannot speak strictly of an o-wave or an e-wave as in uniaxial crystals. In general, the locus of phase-match directions in a biaxial crystal has no simple form and is dependent on the magnitude and combination of the refractive indices taking part in the particular nonlinear process. In a biaxial case, the optics axes lie symmetrically about the z-axis in the x-z plane (optic plane) at a certain angle and coalesce into the z-axis or x-axis for the degenerate case of uniaxial positive or uniaxial negative, repectively.[34] For biaxial positive crystals $n_y < (n_x + n_z)/2$ and for biaxial negative crystals $n_y > (n_x + n_z)/2$. This is consistent with the uniaxial limit, described above, where the optic axis is traditionally taken as the mathematical polar axis. The situation thus simplifies to that in a uniaxial crystal.

➢ Types of phase-matching:

Phase-matching can be achieved by angle tuning, temperature tuning or other methods. If the angle between the optic axis and the propagation vector, θ_m, is 90^0 or 0^0 degrees for negative and positive crystal, respectively, then the phase matching is termed as non-critical phase-matching. It is obtained in some crystals by varying the temperature of the crystal. The cases when the angle θ_m is not equal to 90^0 or 0^0 is called the critical phase-matching where two possible configurations of fundamental interaction can occur.

114

In type-I phase matching, the fundamental is composed of only one principle polarisation component of the incident field [E^2_j (ω) or E^2_k (ω)], whereas type-II involves two orthogonal polarised components [$E_j(\omega)$ and $E_k(\omega)$]. These two types of phase matching are illustrated in Fig. 4.1.3. In Type-I phase matching [Fig. 4.1.3 (A)] the two fundamental waves $E_1(\omega)$ and $E_2(\omega)$ are polarised perpendicular to the optic plane (ordinary waves) and the resultant second harmonic wave $E_3(2\omega)$ is polarised in the optic plane (extraordinary wave). In Type-II phase matching [Fig. 4.1.3 (B)] the two fundamental waves are polarised orthogonal to each other; one polarised perpendicular to and one polarised in the optic plane. The resultant second harmonic wave is polarised in the optic plane (extraordinary wave).

The propagation of fundamental and second harmonic fields, represented in terms of the conservation of momentum, is given by the wave vector mismatch

$$\Delta k = k_3^{(2\omega)} - k_2^{(\omega)} - k_1^{(\omega)} = \frac{2\pi}{\lambda_\omega} \left[2n_3^{(2\omega)} - n_2^{(\omega)} - n_1^{(\omega)} \right] \qquad (4.1.6)$$

in which $k_1^{(\omega)}$, $k_2^{(\omega)}$ and $k_3^{(2\omega)}$ are the moduli of the three collinear wave vectors. A prerequisite for efficient second harmonic generation is that $\Delta k = 0$. For second harmonic generation $\omega_3 = 2\omega_1$ and $\omega_1 = \omega_2$. Hence

$$\Delta k = k_3^{(2\omega)} - 2 \cdot k_1^{(\omega)} = \frac{4\pi}{\lambda_\omega} \left[n_3^{(2\omega)} - n_1^{(\omega)} \right] = 0$$

As discussed later (equation 4.1.10), the SH power $p_{2\omega} \propto p_\omega^2 \operatorname{sinc}^2\left(\frac{\Delta k l}{2}\right)$ When the overall wave vector mismatch $\Delta k = 0$, phase matching is achieved which gives rise to

constructive second harmonic interference as $\mathrm{Sin}\left(\dfrac{\Delta kl}{2}\right)=1$. When this condition is fulfilled, the SH maintains a fixed phase relationship to the non-linear polarisation and is able to extract energy most efficiently from the fundamental field. From a microscopic point of view, we see that the individual atomic dipoles that constitute the material system are in phase so that the SH field emitted by each dipole adds coherently in the forward direction $\left[2\vec{k}(\omega)\rightarrow\vec{k}(2\omega)\right]$. The total power radiated by the collection of all the dipoles thus scales as the square of the number of atoms that participate (constructive interference), which in turn scales with the length of the crystal—hence the L^2 dependence. A measure of the maximum length of a crystal, or coherence length (l_c), that is useful in producing SH power is given by Yariv.[31]

$$l_c = \frac{2\pi}{\Delta k} = \frac{\lambda}{4\left(n^{2\omega} - n^{\omega}\right)} \qquad (4.1.7)$$

From this equation it can be seen that the coherence length can be infinite when Δk goes to zero. In birefringent crystals exact phase matching is usually achieved by angle tuning and in some cases by temperature tuning, which utilises the temperature dependence of the refractive indices.

For second harmonic generation, it is customary reduce the (3 X 9) d_{ijk} tensor in equation (4.1.2) to a (3 X 6) d_{ij} nonlinear tensor: [16, 34]

116

$$\begin{bmatrix} P_x(2\omega) \\ P_y(2\omega) \\ P_z(2\omega) \end{bmatrix} = \varepsilon_0 \begin{bmatrix} d_{11} & d_{12} & d_{13} & d_{14} & d_{15} & d_{16} \\ d_{21} & d_{22} & d_{23} & d_{24} & d_{25} & d_{26} \\ d_{31} & d_{32} & d_{33} & d_{34} & d_{35} & d_{36} \end{bmatrix} \cdot \begin{bmatrix} E_x^2(\omega) \\ E_y^2(\omega) \\ E_z^2(\omega) \\ 2E_y(\omega)E_z(\omega) \\ 2E_z(\omega)E_x(\omega) \\ 2E_x(\omega)E_y(\omega) \end{bmatrix} \quad (4.1.8)$$

From equation 4.1.8 it can be seen that there are maximum number of 18 independent tensor elements. By Kleinman symmetry the maximum number of the independent tensor is further reduced to 10.[16] It is also known that crystals that have a centre of symmetry cannot exhibit a second-order polarisation. Of the 32 different crystal classes, 21 are non-centrosymmetric, but of these only one has no symmetry at all: this is class 1 in the triclinic system. For all the other classes there are one or more symmetry operations, which transform the crystal into itself. As a result of this, certain components of the matrix must be zero, and others are equal or numerically equal but opposite in sign. The ZTS crystal belongs to the orthorhombic structure of class mm2.[36] Such crystals are invariant under an 180^0 rotation about the z-axis. Under such a rotation, a field E_x applied in the +x direction transforms to one applied along the –x direction. As a result, $+d_{111}E_x{}^2$ has to equal $-d_{111}E_x{}^2$. This can only be so if d_{111}=0. Using all such symmetry operations for the orthorhombic structure of class mm2, the second order polarization is uniquely characterized by equation 4.1.9 Tables listing the configurations of nonlinear tensor elements for all 21 crystal classes having no centre of symmetry can be found in most nonlinear optics texts.[16, 28, 34, 31]

$$
\begin{bmatrix} P_x(2\omega) \\ P_y(2\omega) \\ P_z(2\omega) \end{bmatrix} = \varepsilon_0 \begin{bmatrix} 0 & 0 & 0 & 0 & d_{15} & 0 \\ 0 & 0 & 0 & d_{24} & 0 & 0 \\ d_{31} & d_{32} & d_{33} & 0 & 0 & 0 \end{bmatrix} \cdot \begin{bmatrix} E_x^2(\omega) \\ E_y^2(\omega) \\ E_z^2(\omega) \\ 2E_y(\omega)E_z(\omega) \\ 2E_z(\omega)E_x(\omega) \\ 2E_x(\omega)E_y(\omega) \end{bmatrix} \qquad (4.1.9)
$$

By inspection, the interactions for type-I phasematching correspond to d_{31}, d_{32}, and d_{33} nonlinear coefficients, whereas type-II occurs for d_{15} and d_{24}. It can be seen from figure 4.1.3 that for Type I interactions only one of the terms $E_x^2 (\omega)$, $E_y^2 (\omega)$ or $E_z^2 (\omega)$ in equation 4.1.8 can survive. Thus for this type of interactions the relevant non-linear coefficients can be d_{31}, d_{32} or d_{33} Similarly for Type II only one of the terms $E_x(\omega) E_y(\omega)$, $E_y(\omega) E_z(\omega)$, or $E_z(\omega) E_x(\omega)$ in equation 4.1.8 can survive. Thus for this type of interactions the relevant non-linear coefficients are d_{24} or d_{15}.

Efficient non-linear conversion requires not only the phase-matching conditions to be satisfied for the wavelengths of interest, but that the non-linear optical coefficient corresponding to the chosen polarisation configuration is large. This can be seen in the expression for the internal SH conversion efficiency[31]

$$
\eta \equiv \frac{P_{2\omega}}{P_\omega} = \frac{8\pi^2 d_{\text{eff}}^2}{n_\omega^2 n_{2\omega} c \varepsilon_0 \lambda_\omega A_{\text{ovl}}} p_\omega L^2 \text{sinc}^2\left(\frac{\Delta k L}{2}\right) \qquad (4.1.10)
$$

where $P_{2\omega}, P_\omega$ are the powers of the second harmonic and fundamental, d_{eff} is the effective non-linear coefficient, L is the length of the crystal, and A_{ovl} is the effective area of cross-section of the fundamental field inside the crystal.

If d_{eff} were the only important quantity to be considered in a nonlinear interaction figure of merit, it would only be necessary to find the direction of propagation vector,
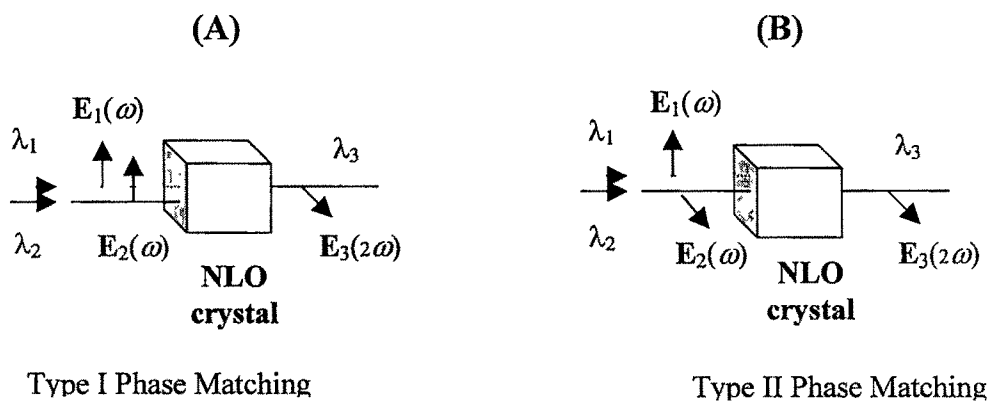
(A)   **(B)**

Type I Phase Matching   Type II Phase Matching

Figure 4.1.3. Type-I **(A)** and Type-II **(B)** phase matching schemes are shown. In Type-I phase matching the two fundamental waves $E_1(\omega)$ and $E_2(\omega)$ are polarised perpendicular to the optic plane (ordinary waves) and the resultant second harmonic wave $E_3(2\omega)$ is polarised along the optic plane (extraordinary wave). In Type-II phase matching the two fundamental waves are polarised orthogonal to each other; one polarised perpendicular to and one polarised in the optic plane. The resultant second harmonic wave is polarised in the optic plane (extraordinary wave).

which maximize this quantity. This can be a tedious task, especially if the crystal happens to be a biaxial, partly because of the complicating effects of the finite polarization offsets for each wavelength, and partly because of the skew walk- off directions of the ordinary and extraordinary rays, compared to the uniaxial case. In general, d_{eff} undergoes several peaks and valleys (and nulls) as one traces the entire phase-matching locus for a given interaction, and not all of the peaks are necessarily equal.[37]

4.1.3. Second Harmonic Generation in ZTS

Zinc (tris) Thiourea Sulphate as mentioned earlier comes from the class of Semiorganics, a class of materials which has been know for years and investigated for their NLO properties. ZTS crystallises in the non-centrosymmetric orthorhombic point group mm2 from aqueous solutions as colourless block like crystal with the crystallographic and principle dielectric axes normal to the natural growth faces. The X-ray structure determination shows the zinc ion terahedrally co-ordinating three planar thiourea molecules and one oxygen from a sulphate.[36] There is also extensive inter- and intramolecular hydrogen bonding between thiourea N-H's and the sulphate O's, and this feature most likely gives rise to the noncentrosymmetry.[38]

The refractive indices of ZTS suggests that the crystal is nearly uniaxial negative. This is evidenced by the fact that the indices for propagation along the crystallographic a–axis (y-axis or [100]) and c-axis (z-axis or [001]) being nearly equal ($n_a \sim n_c$) within experimental uncertainty at 1.782, while that along the b-axis is 1.701 at 600nm.[38, 34] The transmission spectrum for a ZTS crystal shows a UV cut-off below 0.300 μm. Also the spectrum indicates a shallow N-H vibrational overtone absorption at ~ 1.040 μm. Deutrating the material has been shown to results in a shift of the 1.040 μm absorption peak by ~ 0.400 μm towards longer wavelengths.[39] A similar situation occurs in d-urea and d-ammonium dihydrogen phosphate (AD*P).[40] However, careful refractive index measurements along with an analysis of the nonlinear coefficient tensor show that d- ZTS will not noncritically phase match for second harmonic generation despite the promise

shown by the its undeuterated analog.[41] In addition, the acceptance angle even for critical phase matching is very small.

There are few reports on the second harmonic generation in ZTS.[42, 38, 39] They report on powder method evaluation of the type-I and type-II phase matching loci in this crystal. The values of effective second order nonlinear optical coefficient (d_{eff}), the acceptance angle (βo) and the damage threshold for SHG were also reported.[43,44] The work reported by H. O. Marcy and co-workers concentrates on second harmonic generation of the 1064 nm output of the Nd: YAG laser. Unfortunately, the N-H vibration overtone absorption peak at ~1040 nm mentioned above makes the standard (undeutrated) ZTS crystals almost useless for fundamental inputs at 1064 nm.

The standard ZTS crystals are suitable candidates for SHG for fundamental inputs in the 600-1000 nm wavelength region where the effects of the 1040 nm absorption peak are minimal. In this thesis, we report a Type-I second harmonic generation in as-grown ZTS crystals with near-IR fundamental inputs between 820 and 950 nm from a femtosecond laser. An estimate of the effective non-linear coefficient, d_{eff}, is determined by comparing the second harmonic response of the ZTS crystals with beta barium borate (BBO) crystal.

4.1.3.1. Experimental Set-up

The experimental work discussed here was performed at the Applied Optics Centre of Delaware, Delaware State University, USA. The source of fundamental infrared (IR) used for study of SHG in ZTS is tuneable argon pumped Titanium: Sapphire laser (*Coherent MIRA-900F*). This laser is tuneable in the ~ 720-980 nm wavelength

range. In continuous wave (CW) mode, the bandwidth of the laser is ~2 nm. In modelocked conditions, the laser produces ~ 100 fs pulses at a repetition rate of 76 MHz. The ZTS crystals used under study were as grown and were not cut or polished.

The experimental set-up for the study of SHG in ZTS is shown in Figure 4.1.4. The IR beam from the Ti: Sapphire laser is horizontally polarised. As shown in the side view in figure 4.1.4, two mirrors mounted at 45^0 relative to the vertical switches the polarisation of the beam so that the beam incident on the sample is vertically polarised. The ZTS sample is mounted on a rotation stage with the axis of rotation parallel to the [100] direction. The beam enters the sample crystal through the (012) face and exits through the (001) face. The exiting beam is incident on a polarising beamsplitter cube, which separates the vertically and the horizontally polarised components of the beam. This is done because in type-I phase matching, the SH beam (2ω) is expected to be horizontally polarised when the fundamental beam (ω) is vertically polarised. To eliminate the residual IR, SH beam is passed through two filters, a hot mirror (interference filter that reflects > 95 % of the IR) and a blue filter. Two photo-detectors (LM2 photodiode sensors from Coherent, Inc.) measure the input fundamental and the SH powers.

All phase matching angles for ZTS are measured relative to the [012] direction as described in the following procedure. The sample is rotated so that the IR reflection from the (012) face is retro-reflected along the incidence direction. This angle is noted on the rotation stage and corresponds to the [012] direction. The sample is then rotated to optimise the second harmonic output at a given wavelength. This angle is recorded and the difference from the angle corresponding to the [012] direction is calculated. This
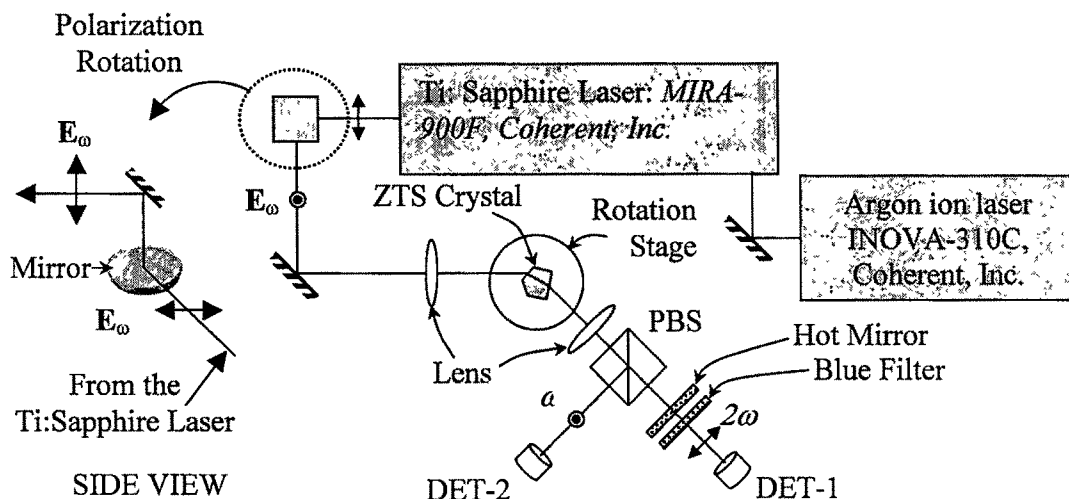
123

Figure 4.1.4. Top view of the experimental set-up for second harmonic generation study. The fundamental beam from a tuneable Ti: Sapphire laser is focused onto the crystal. The polarization beamsplitter cube (PBS) separates the horizontally polarized second harmonic output (ω) from the vertically polarized fundamental (2ω). The hot mirror and the blue filter eliminate any residual traces of the fundamental beam.

gives the phase matching angle relative to the [012] direction in air. The corresponding angle inside the crystal can be calculated using Snell's law.

4.1.3.2. Results and Discussion

One of the important properties of a non-linear material is that it should be phase-matchable over the range of interaction frequencies. In other words, the crystal must be sufficiently birefringent to compensate for dispersion and thus allow phase matching. The degree of birefringence of the crystal and its phase-matchability can be determined from the refractive index data at appropriate wavelengths, which may be obtained from the dispersion relation. Such a relation, the so-called Sellmeier equation, for the material can be expressed as

$$n = \sqrt{A + \frac{B}{\left(\lambda^2 - C\right)} - D \cdot \lambda^2}$$

(4.1.11)

where A, B, C, and D are the Sellmeier coefficients n is the refractive index and λ is the wavelength. The Sellmeier coefficients are usually determined empirically. For ZTS the Sellmeier coefficients, determined by a least-square fit to the measured refractive-index data, were reported by H. O. Marcy et al.[39] This data was used by the author to compute the optical indicatrix and the phase matching directions for SHG studies reported below.

> **Phase-matching direction in ZTS**

The present study demonstrates type-I SHG from fundamental inputs in the 800-950 nm wavelength range. For ZTS sample, the highest second harmonic output is obtained at 920 nm. Therefore, phase matching in ZTS at 920 nm is discussed in detail.
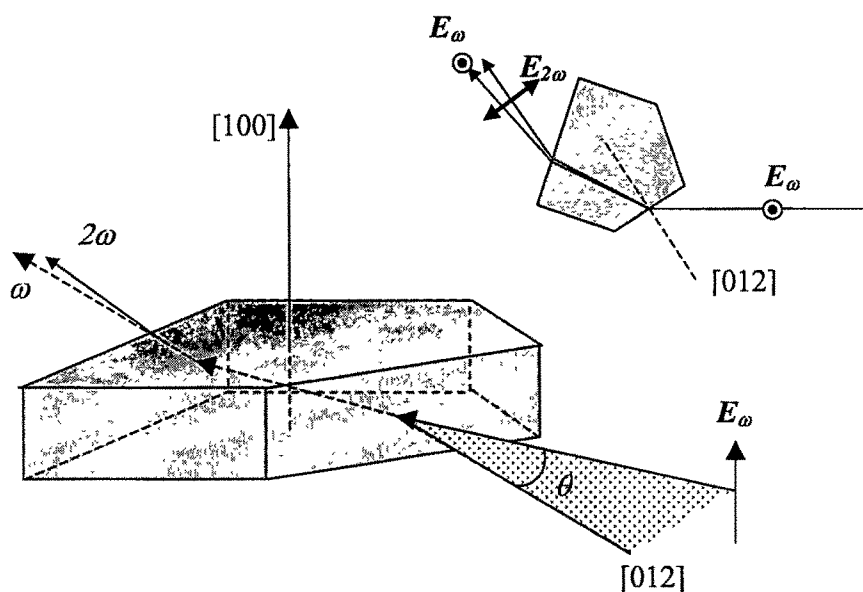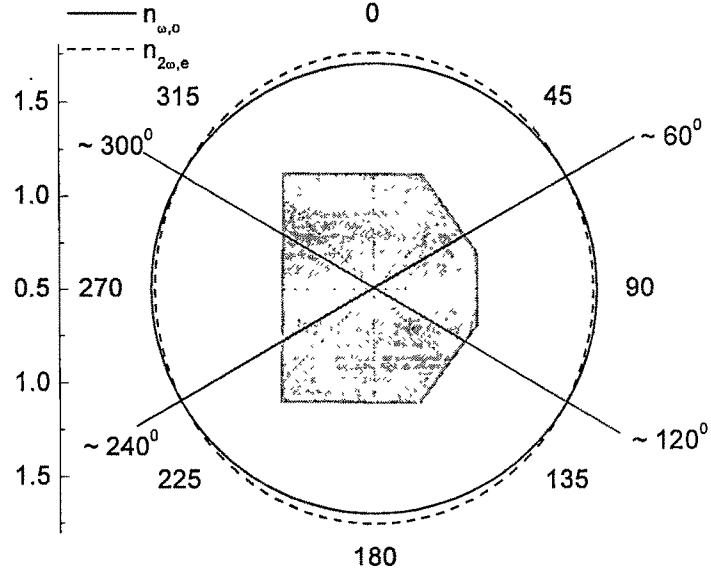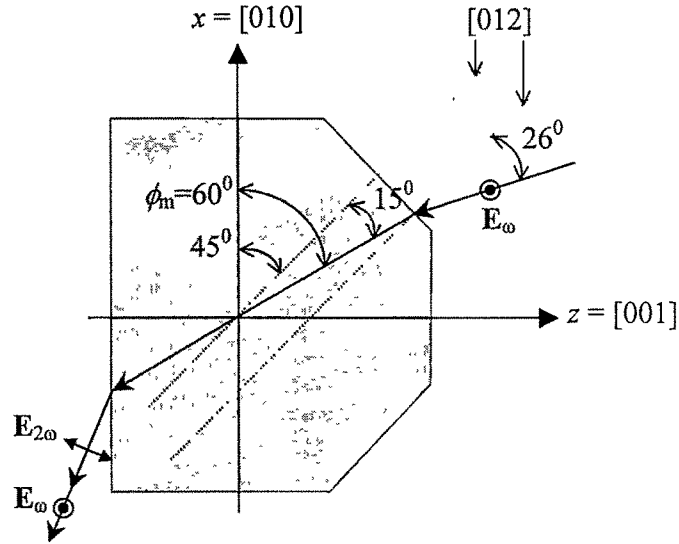
Figure 4.1.5. The propagation direction of the fundamental and the second harmonic and their respective polarizations are indicated in the figure. θ is measured to be nearly 27^0 relative to the [012] direction for optimum SH power at 920 nm.

(a)

(b)

Figure 4.1.6. (a) The figure shows a polar plot of the variation of refractive index with the direction of propagation in the x-z plane. The solid line represents the refractive index for the fundamental wave at 920 nm polarised along the y ([100])-direction while the dotted line represents the second harmonic wave at 460 nm polarised in the (100) plane. The solid radial lines at $\phi_m \sim 60^0$, 120^0, 240^0 and 300^0 indicate the phase matching directions where $n_e^{2\omega} = n_0^\omega$. The shaded form in the background indicates the orientation of the crystal. **(b)** The process of second harmonic generation at the phase matching angle $\phi_m \sim 60^0$ is shown along with the direction of propagation and the polarisation directions of the fundamental and second harmonic waves. The dotted lines indicated the [012] direction.

128

matching in ZTS can be described differently. Figure 4.1.7 illustrates this description, which shows the Sellmeier plots for ZTS for wavelengths between 350 and 1000 nm. The fundamental beam (ordinary wave) corresponds to $n_o = n_y(920\text{nm}) \sim 1.698$. The SH beam (extraordinary wave) corresponds to $n_e(460\text{nm})$. The extraordinary refractive index at $\phi_m = 60^0$ for 460 nm can be estimated using equation 4.1.6 as shown below.

$$\frac{1}{n_e^2\left(60^0\right)} = \frac{\cos^2 60^0}{n_z^2} + \frac{\sin^2 60^0}{n_x^2}$$

Using $n_z = n_z(460 \text{ nm}) = 1.753$ and $n_x = n_x(460\text{nm}) = 1.678$ this equation yields $n_e^{2\omega}(\phi_m = 60^0) \cong 1.698$. Thus $n_o(920 \text{ nm}) = n_e(460 \text{ nm}) = 1.698$.

Since the transparency of the crystals extends down to $\sim$ 300 nm, there is every reason to expect phase matching for fundamental wavelengths up to 600 nm. However such a phase matching will require appropriate cutting of the crystal. The uncut ZTS crystals, were found to be phase-matchable over a large near-infrared wavelength range as shown in Figure 4.1.8. The figure shows the measured phase-matching angle θ (in air) as a function of the fundamental wavelength. The angle θ is measured from the [012] direction. The as-grown ZTS crystal is phase-matchable over a range of wavelength that spans from about 880 to 980 nm. This requires rotation of the crystal by nearly 25 degrees. Clearly the extension of phase matching over a wider range of wavelength will require appropriate cutting of the crystal.

➤ **Angle Tuning**

As mentioned earlier, in most cases one can achieve phase matching with the aid of angle tuning and utilising the natural birefringence of the media to compensate for
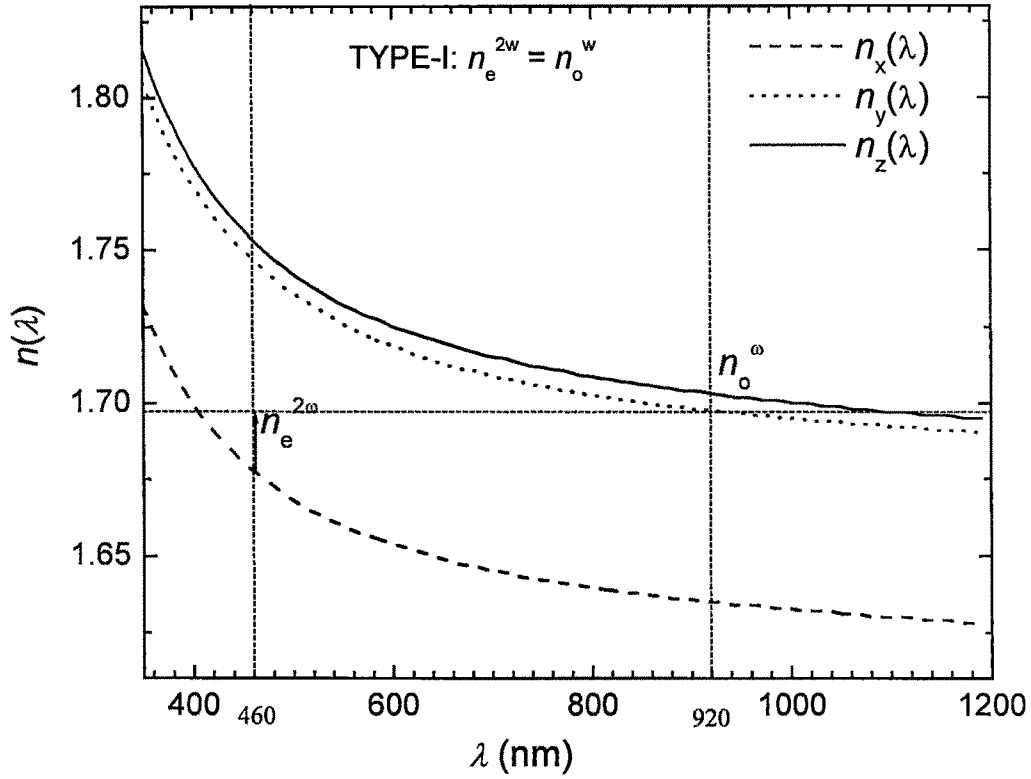
Figure 4.1.7. Sellmeier plots for ZTS in the 350-1200 nm wavelength range. The indices $n_y(\lambda)$ and $n_z(\lambda)$ are nearly equal indicating a nearly uniaxial nature of the crystal. Type-I phase matching, is indicated at 920 nm producing a second harmonic output at 460 nm. Ref 39
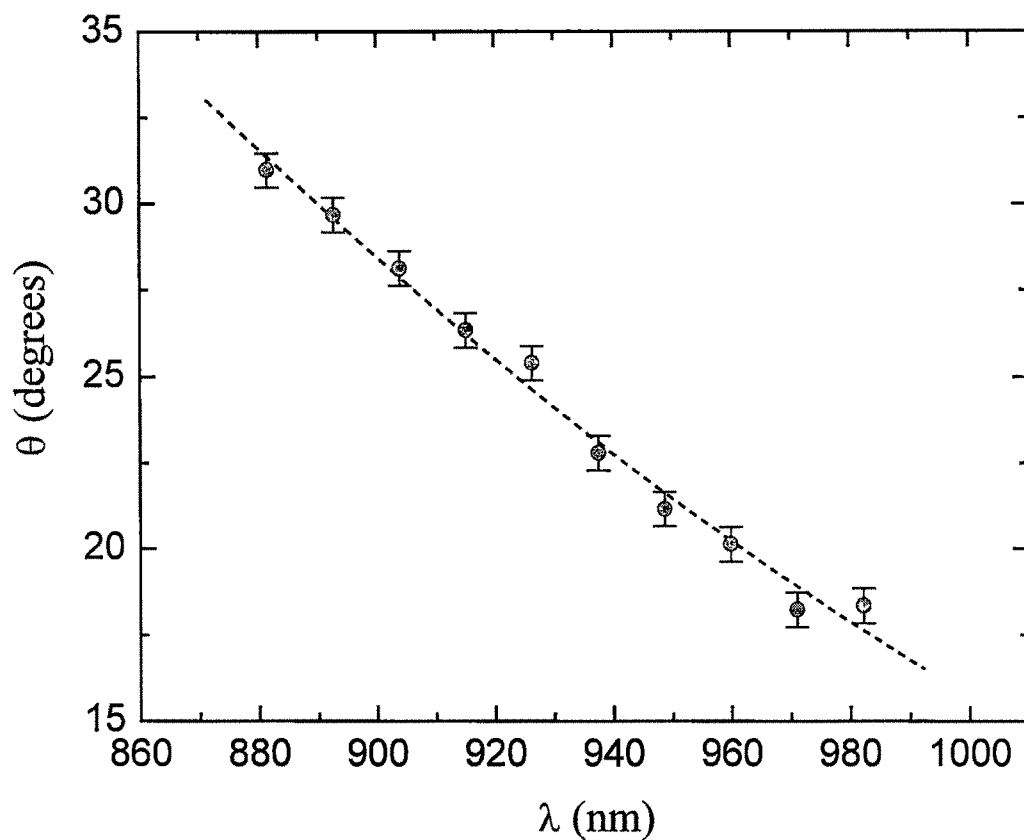
Figure 4.1.8. The phase-matching angles are indicated as a function of wavelength. The angle θ (in degrees) is measured from the [012] direction. The as-grown uncut ZTS crystals were found to be type-I phase-matchable over a range of nearly 100 nm wavelength range in the near infrared region. Phase-matching for an extended wavelength range requires appropriate cutting of the crystal.

dispersion such that $n(\omega) \approx n(2\omega)$ to eliminate phase mismatch. A variation of the angle between the wave vector and the crystallographic x-axis results in a change of the refractive index of extraordinary wave. Thus, one can transmit the wave at an angle ϕ_m to the x-axis, such that the refractive index for the input, polarized as an ordinary ray, is exactly equal to the refractive index for the second harmonic polarized as an extra-ordinary ray. This can be achieved for all wavelengths for which the ordinary index is larger than the extraordinary index at $\lambda/2$.[45] The angular sensitivity of femtosecond SHG in ZTS crystals is also reported in this thesis. The results are shown in Figure 4.1.9. The measured full-width half maximum (FWHM) of SHG, which is the angular acceptance bandwidth, is an important parameter because it determines the angular tolerance needed to maintain optimum output of the frequency conversion device. The angular acceptance bandwidth for ZTS is about 0.73^0 while that for BBO is 0.37^0 shown in figure 4.1.9. Thus the angular bandwidth for ZTS is almost twice that of BBO. This is a desirable characteristic because the SHG output is less sensitive to small changes in crystal orientation.

> **Conversion efficiency**

The conversion efficiency of the ZTS crystals is an important parameter to be considered. There are several measures of conversion efficiency. The author uses the simplest definition of conversion efficiency, η, given by Equation 4.1.10. The highest conversion efficiency is obtained at around 920 nm. For our samples, the best conversion efficiency recorded for femtosecond input is measured to be of the order of 10^{-3} for a crystal with length of 4 mm. A commercial BBO crystal of length 7 mm, with surfaces
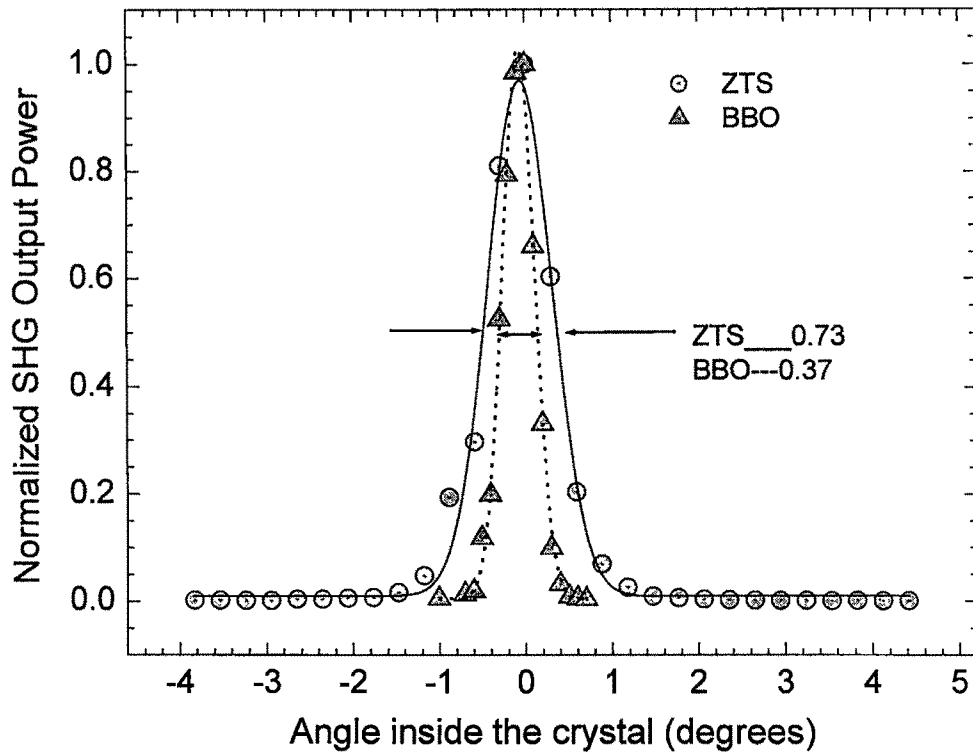
Figure 4.1.9. The angular sensitivity of second harmonic generation for ZTS and BBO is shown in the figure. 0° degrees on the x-axis represent the phase-matching direction for both crystals at which the maximum SHG is observed. The angles shown are those calculated inside the crystal by using Snell's law. The input fundamental is a 76 MHz train of ~ 100 femtosecond pulses at 920 nm wavelength. The femto-second angular acceptance for ZTS is about 0.73 degrees while that for BBO is about 0.37 degrees.

polished and antireflection-coated, yielded an efficiency of the order of 10^{-2} under the same conditions.

➤ Estimation of the effective nonlinear coefficient, d_{eff}

This section describes the determination of the nonlinear coefficient, d_{eff}, for the ZTS crystal. This parameter gives an estimation of the expected second harmonic output that can be achieved. The power of second harmonic output in a nonlinear optical crystal is given by:[31]

$$P^{(2\omega)} = 8\left(\frac{\mu_o}{\varepsilon_o}\right)^{\frac{3}{2}} \frac{\omega^2 d_{eff}^2}{n_\omega^2 \cdot n_{2\omega}} L^2 \left[\frac{\{P^{(\omega)}\}2}{\pi\omega_o^2}\right] \frac{Sin^2\left(\frac{\Delta K * L}{2}\right)}{\left(\frac{\Delta K * L}{2}\right)^2} \qquad (4.1.12)$$

where $P^{(\omega)}$ is the input fundamental power, ω is the angular frequency, $n = (n_\omega = n_{2\omega})$, L is the interaction length, ΔK is the wave vector mismatch, μ_o is permeability constant and ε_o is the permittvity constant of free space. The beam focusing geometry is characterised by the minimum beam waist ω_0 and the Rayleigh range $2z_0$. These quantities are indicated in Figure 4.1.10. Direct determination of the absolute d_{eff} is difficult. It can be seen from Equation 4.1.12 that the determination of d_{eff} is extremely sensitive to the exact beam parameters such as the effective area of interaction determined by the Gaussian beam parameters.
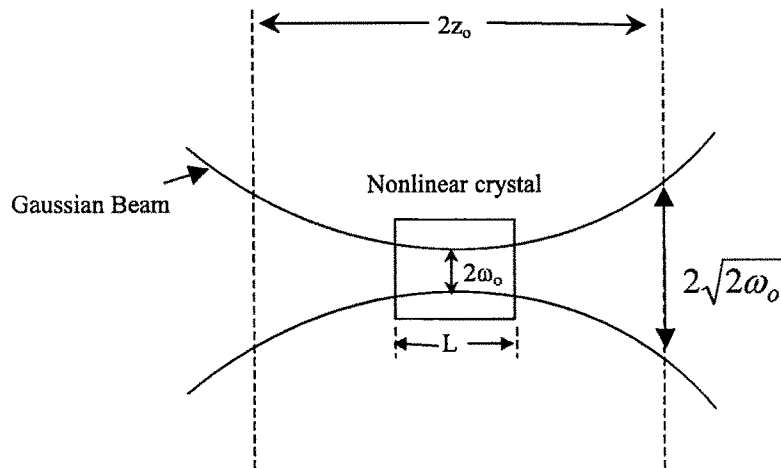
Figure 4.1.10 Gaussian beam focused inside a nonlinear optical crystal. L is the length of the crystal. The beam focusing geometry is characterised by the minimum beam waist ω_o and the Rayleigh range $2z_o$ Ref [31]

The work presented below is only an estimation of the effective non-linear coefficient. An alternative to direct determination of d_{eff}, is to compare the SH output of the ZTS crystals with that obtained from another well-known crystal such as BBO under the same experimental conditions. Using the experimental set-up described above the fundamental and second harmonic powers are measured for both ZTS and BBO. Using Equation 4.1.12, the ratio of the SH powers for ZTS and BBO can be expressed as

$$\frac{P_{ZTS}^{(2\omega)}}{P_{BBO}^{(2\omega)}} = \left(\frac{d_{ZTS}}{d_{BBO}}\right)^2 \left(\frac{L_{ZTS}}{L_{BBO}}\right)^2 \left(\frac{n_{BBO}}{n_{ZTS}}\right)^3 \left(\frac{P_{ZTS}^{(\omega)}}{P_{BBO}^{(\omega)}}\right)^2 \qquad (4.1.13)$$

This yields

$$d_{ZTS} = \sqrt{\frac{P_{ZTS}^{(2\omega)}}{P_{BBO}^{(2\omega)}} \left(\frac{L_{ZTS}}{L_{BBO}}\right)^2 \left(\frac{n_{BBO}}{n_{ZTS}}\right)^3 \left(\frac{P_{ZTS}^{(\omega)}}{P_{BBO}^{(\omega)}}\right)^2} * d_{BBO} \qquad (4.1.14)$$

This assumes that the entire length of the crystals L_{ZTS} and L_{BBO} are used. For femtosecond pulses, this is not very easy to accept but can be used for estimation of d_{eff}. The beam focusing parameters being the same for both crystals (ZTS and BBO) cancel out in the above calculation. The values of the effective nonlinear coefficient, d_{eff}, were determined for several ZTS crystal samples by comparison with BBO. A statistical evaluation of d_{eff} for ZTS is shown in table 4.1.1.

The estimated d_{eff} from these calculations can be reported to be 0.3 ± 0.1 pm/V. This number is close the value of ~ 0.2 pm/V determined by powder method for type-I SHG at 1064 nm reported by H. O. Marcy, et al.[39]

Table 4.1.1: Determination of d_{eff}.

$(d_{eff})_{BBO}$ = 1.47 pm/V[37], L_{BBO}=7 mm						
Sample No.	λ (nm)	L_{ZTS} (mm)	$P_{ZTS}(\omega)$ (mW)	$P_{ZTS}(2\omega)$ (μW)	$P_{BBO}(\omega)$ (mW)	$P_{BBO}(2\omega)$ (mW)	$(d_{eff})_{ZTS}$ (pm/V)
1	920	7	97	25.2	97	5.96	0.286
2	850	3	178	124	292	35.3	0.347
3	920	5	204	243	217	34.9	0.201
Average $(d_{eff})_{ZTS}$ = 0.3± 0.1 pm/V							

Other quantities that can affect the determination of d_{eff} are the reflections at the input and the exit surfaces of the crystals. The BBO crystal used for this comparative study has both these surfaces anti-reflection coated for the near infrared wavelength range. This is not the case for the ZTS crystals. However, it must be emphasised that a measure of the fundamental power actually following these two reflections is being recorded by detector 1 (DET 1) shown in Fig. 4.1.4 for both the crystals. This minimises the uncertainty due to surface reflections. However, the surfaces of the ZTS crystals used for this study were not polished. In addition, the SH output for the BBO crystals is obtained at near normal incidence. This could lower the estimated value of d_{eff} for ZTS. Furthermore, femtosecond pulses effectively use a shorter length of the crystal, which is typically of the order of a few hundred microns.

➤ **Device Considerations**

Several factors need to be considered when constructing a frequency-doubling device using ZTS crystals. Such a device has not been implemented in this dissertation. The loss of both the fundamental and the second harmonic power due to reflection,

scattering from defects, etc. in the crystal should be minimised. The quality of the crystal itself determines the loss due to absorption and scattering due to defects. Further the input and exit surfaces of the crystal can account for loss of power. Therefore the crystal needs to be polished and appropriately cut to yield maximum SH power. Proper anti-reflection coating should be applied on the surfaces to prevent reflections. As ZTS crystal is grown by aqueous solution growth, it is possible that the crystal can be affected by moisture. A similar problem is encountered in the case of KDP. KDP crystals are typically mounted in a sealed housing with transparent windows at the input and output ends to prevent moisture from condensing on their surfaces. This technique can be used for the ZTS crystal to prevent surface damage due to moisture. It must also be noted that a detailed study of appropriate focusing conditions was not carried out in this work. These conditions can significantly enhance the second harmonic generation in these crystals. Further, thinner crystals are needed for femtosecond SHG to prevent excessive group velocity dispersion of the ultra-fast pulses. Lastly, the crystals must be mounted in the device after appropriate consideration of its hardness and thermal expansion properties to prevent cracking of the crystal due to thermo-mechanical factors during high power laser irradiation.

4.1.4. Conclusions

A preliminary study of Second Harmonic Generation in Zinc (tris) Thiourea Sulphate (ZTS) under femtosecond fundamental input is discussed in this section. This study shows for the first time that type I phase matching is possible in ZTS over a wide range of input wavelengths. Phase matching angles are measured in this study between 820 and

950 nm. This range can be extended by appropriately cutting the as-grown ZTS crystal. The femtosecond SHG angular acceptance is measured to be $\sim 1.3^0$. The effective nonlinear coefficient is estimated to be 0.3 ± 0.1 pm/V. This value is obtained by comparison of SHG outputs from a BBO crystal. Without cutting or polishing the as-grown ZTS crystals second harmonic output of ~ 0.3 mW is obtained with 100 fs femtosecond input at 76 MHz repetition rate and ~ 500 mW average power. This output can be enhanced by appropriately cutting and polishing the crystal and by application of antireflection coatings to minimize loss at the input and the output surfaces.

4.2. Laser damage

4.2.1. Introduction

As applications of non-linear optical materials in laser technology can involve high optical intensities, it is essential to study the damage caused by intense laser irradiation on to these materials. When a low intensity light beam passes through a transparent substrate or falls on a reflecting mirror or on an absorbing medium, no damage occurs because the field strength is lower than the bonding energies in the material. As the intensity of the beam increases a whole range of reversible interactions may occur obvious. These include strain, distortion, expansion, thermal effects, non-linear transmittance and absorption, electro-optic effects, and self-focusing. When the intensity of the beam is increased beyond some threshold value, non-reversible changes in the material or component begin to occur. These include cracking, pitting, melting, vaporisation and violent shattering. The first laboratory laser systems were bulky and frequently unsuitable for many industrial and military applications. In recent times there was an increased demand for high efficiency and reduction in the system size. This inevitably leads to the occurrence of energy and power densities that would damage the components and compromise the laser resonators. Several effects, such as absorption, distortion and laser-induced damage, which modify the output of the laser are important and must be taken into account.

A little more than 30 years have passed since the first observation of optical breakdown in transparent solids.[46],[47] The laser damage research field is enormous and includes physical problems of the interaction of high power laser radiation with matter

and various physical, chemical, mechanical, optical, and other aspects of material technology for high-power laser optics. From the very beginning of the laser damage research a large number of possible mechanisms and models of damage under high-power laser radiation have been discussed in the literature.

4.2.2. Laser Damage Background

4.2.2.1. Laser Damage Mechanisms

For materials that have high absorption at the laser wavelength, the mechanisms that result in damage are totally energy-dependent and breakdown results from cumulative thermal effects. On the other hand, for materials that are highly transparent at the laser wavelength the damage mechanisms mainly depend on the peak power density. Thus laser damage mechanisms can be classified in two broad categories discussed below. A detailed discussion of several specific mechanisms can be found in Ref. [48].

1. Dielectric Breakdown:

The electric field, $E(t)$, of a light beam passing through the solid induces a polarisation, $P(t)$, which results from separation of the charges in the medium schematically shown in Figure 4.2.1. At electric fields comparable to the atomic electric field, the local homogeneous arrangement of ions is disrupted. This is referred to as dielectric breakdown.

2. Thermal Absorption

In absorbing materials, laser irradiation leads to local heating that depends on the relative rates of laser energy absorption and the diffusion of heat in the material. Since

diffusion of heat in most materials can take place over several milliseconds, all energy deposited during this duration contributes to local heating. This can lead to intense local heating and consequent local melting of the medium. This local disruption of the homogeneous arrangement of ions often leads to self-focusing effects due to formation of a thermal lens contributing to further damage in the material.

The mechanism of laser damage strongly correlates with several laser parameters. These include the peak power density (spatial and temporal) of the laser pulse, maximum energy density (spatial), average power density in a pulse train, the cw power density and the pulse repetition frequency (PRF) of the laser irradiation.

Figure 4.2.1. Polarisation of the material under the influence of the optical field

The condition of the sample used for laser damage also determines the laser-induced damage threshold (LIDT). Multiple reflections from interfaces, such as crystal surfaces, can interfere and result in higher electric fields. This causes laser damage to occur at power densities that are nominally lower than the bulk (without the presence of interfaces) values. Further any inhomogeneity in the bulk material tends to produce local higher power and energy densities.[49] If a material contains discontinuities, reflections and diffractions occur. The material (bulk or surface) can break down at a lower LIDT than the intrinsic level.[50] Stimulated Brillouin scattering, which amplifies an acoustic wave and secondary electromagnetic wave at the expense of the input laser beam, can cause damage resulting from the mechanical stresses associated with the acoustic wave. Self-focusing effects result in damage threshold power densities that vary with material length.[51, 52] In the presence of an electric field and electron-phonon collisions; an electron drifts in the direction of the electric field gaining energy. When the electron gains sufficient energy it can excite another conduction electron across the electronic energy gap. Repetition of this multiplication process increases the number of electrons until breakdown occurs when the local temperature is raised to the melting point.[53] This process is referred to as electron-avalanche breakdown and has been discussed in references [54] and [55].

4.2.2.2. Types of Laser Damage Measurements

As discussed earlier, cummulative effects play an important role in laser damage. The following two types of measurements are typically carried out in evaluating the laser damage resistance of an optical material.

1. Single shot measurements

In single shot LIDT measurements, several positions on the sample surface are irradiated with a single shot of known laser power density, stepping clear of each site between pulses and gradually increasing the input laser power until damage can be seen visually.

2. Multi or Cumulative shot measurements

There are several mechanisms, which allow damage to occur at power levels below the single shot threshold level. These measurements can be split into the following two categories.

- **Cumulative damage** is dependent on number of pulses but is independent of pulse repetition frequency (PRF effects). Cumulative damage occurs when small damage sites gradually appear after passage of a number of pulses. The power density levels at which this happens are function of the number of shots, the energy and power densities and the thermal conditioning of the sample under test. More details and specific examples can be found in references 56, 57, 58 & 59.

- **Pulse repetition frequency (PRF)-dependent effects:** At low PRFs the sample temperature rises and falls back to ambient temperature between pulses. At a given PRF, the sample temperature stabilises to a level above the room temperature depending on the thermal diffusivity and dimensions of the sample. For the damage threshold to be PRF dependent, the material must have some absorption at the laser wavelength. It is experimentally shown that for Group II-VI compounds damage is PRF-dependent while for the halides the damage is virtually PRF-independent.[60]

4.2.2.3. Factors affecting the Laser Damage Studies:

One of the requirements for the measurements of laser damage is to have the ability to carefully characterize the source laser.

The **laser wavelength** is one of the most important factors that need to be taken in to account. Presence of specific absorption peaks corresponding to a particular wavelength could lower the damage threshold in the material. As the **spatial characteristics** determine the local power density maxima, a TEM_{00} mode with a Gaussian transverse profile is desirable. The **pulse energy** and **temporal characteristics** determine the peak power of the pulsed laser. The **focusing details** such as focal length, whether the spot is in or out of focus and focal size ($1/e^2$ diameter is suggested) are important for evaluating the quoted irradiation levels. Further, it is necessary to polish the surface of laser windows and mirrors. The surface should be free from defects such as scratches, voids, and digs and this can be achieved by appropriate polishing, cleaning[61] and coating procedures.[62, 63, 64, 65]

4.2.3. Laser Damage Studies on ZTS crystal

There are earlier report of laser damage on ZTS crystals performed using a 1064 nm, 10 Hz, 40 ps pulses from Nd: YAG.[66] This work reports on the laser damage in ZTS crystals at 532nm using a 10 Hz, 10 ns Nd: YAG laser. It is found that, ZTS displays a high damage threshold in the visible that is comparable to the commercially available NLO crystals like KTP and BBO.

4.2.3.1. Experimental

The experimental set up used for laser damage in ZTS is shown in Fig. 4.2.2. A *BMI Industries* Q-Switched Nd: YAG laser is used for this experiment. This laser can be operated in two modes. In the single-shot mode the laser emits a single ~8 ns pulse. In the multi-shot mode the laser produces a continuous train of ~ 8 ns pulses at a repetition rate of 10 Hz, 5 Hz or 2 Hz. The laser generates about 450 mJ/pulse at the 1064 nm fundamental radiation and about 250 mJ of its second harmonic.

The set up used for laser damage studies at 532 nm is shown in Fig. 4.2.2. (a). A wedge beam splitter and a prism combination is used to generate a beam with pulse energies below 2 mJ. This is followed with a neutral density (ND) attenuator wheel to further reduce pulse energies to the desired values. Two detectors A and B shown in the figure are used to monitor the energy of the pulses incident on the ZTS sample. For any particular attenuation of the variable attenuator wheel, the pulse energy of the beam propagating in the direction of the ZTS sample is measured using two detectors A and B. Detector A (LMP2 from *Coherent, Inc.*) is removed and the sample is irradiated with the required number of pulses. During laser irradiation, detector B (LMP10i from *Coherent, Inc.*) keeps a count of the number of pulses and the average pulse energy of the beam incident on the detector. Since the ratio of the two detectors is determined, the pulse energy of the beam incident on the ZTS sample can be calculated. The 5.5 mm diameter beam is focused onto the sample with a 40 cm focal length lens. Using the following relations obtained from Gaussian beam analysis, the focused spot at the sample surface can be calculated.
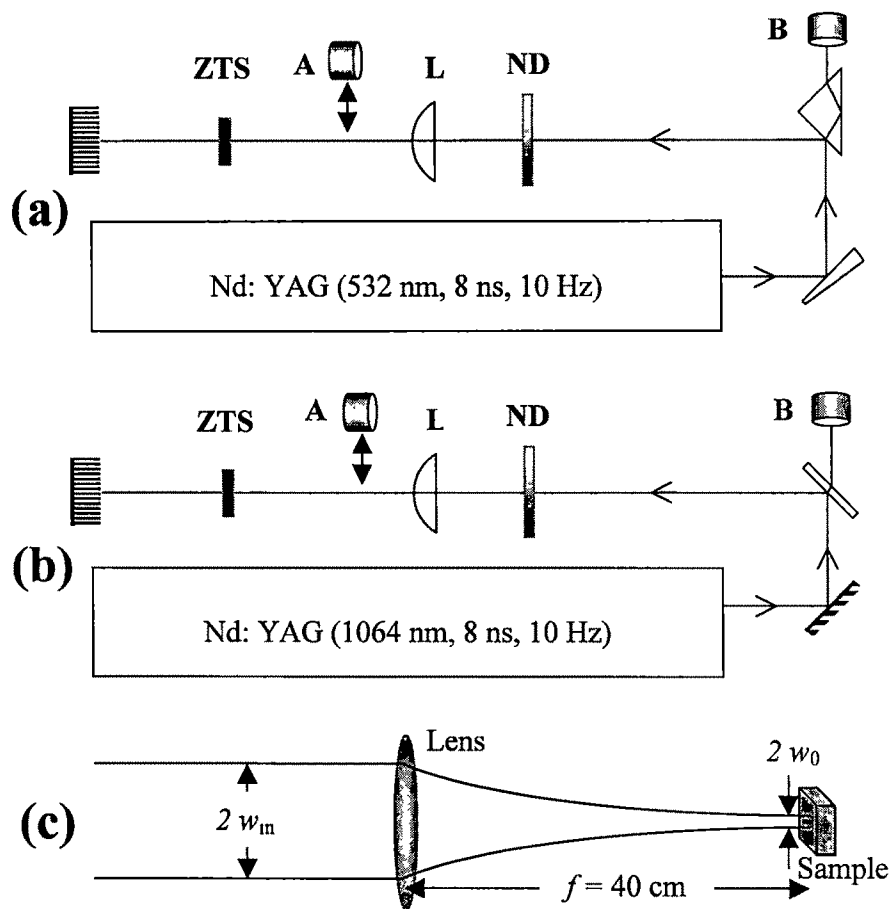
Figure 4.2.2. Experimental set up for laser damage studies.

$$w_0 = \frac{w_{in} \cdot \frac{f}{d}}{\sqrt{1 + \left(\frac{f}{d}\right)^2}}$$

(4.2.1)

where

$$d = \frac{1}{2} \cdot k \cdot w_{in}^2,$$

$$k = \frac{2\pi}{\lambda}.$$

Here w_{in} (= 0.275 cm) is the $1/e^2$-radius of the beam incident on the focusing lens having a focal length f (= 40 cm). These quantities are shown in Fig. 4.2.2. (c). This yields a focused spot with a $1/e^2$-radius w_0 (=25 μm) for a wavelength λ (532 nm). With this arrangement laser intensities up to 10 GW/cm^2 are obtained at 532 nm. A slightly modified set up is used for laser damage studies at 1064 nm and is shown in Fig. 4.2.2. (b). This set up uses a mirror and a 30/70-beamsplitter to generate a beam with pulse energies below 5 mJ. The radius of the laser beam at 1064 nm is measured before the focusing lens using a Kodak Photographic paper. The radius of the focused spot is estimated to be 50 μm using equation 4.2.1. The sample is mounted on a sample holder. Measurements were made on the (100) and (012) face of crystal, which are relevant for second harmonic generation and the laser damage threshold for single as well as multiple shots is estimated. The damage threshold is detected by observing of the sample under a *Wards* microscope.

4.2.3.2. Results and Discussion

The laser damage at 532 nm rendered the crystal useless. The discussion of laser damage at 1064 nm is deferred to the end of this section. This section discusses the damage to the (100) plane of the crystal in detail. A thorough study of the (012) plane was not possible due to the difficulty of growing crystals with a large (012) plane and difficulty of mounting the crystal. However, from measurements on one larger sample the laser damage threshold for the (012) face is estimated to be of the same order of magnitude as the (100) face. The resulting laser damage patterns on the (100) face of the crystal are shown Fig.4.2.3. The determination of laser damage threshold is explained using this figure. The first encircled pattern shows the onset of the damage for 500 shots at 0.1 mJ, (0.43 GW/cm$^{2)}$ and a faint black spot is observed. The second and third circles show the resulting pattern when the pulse energy is increased to 0.3 mJ (1.36 GW/cm^2) and then further to 0.45 mJ (1.75 GW/cm^2), respectively. For our study the onset of laser damage was defined by the appearance of the encircled pattern 1 shown in the figure.

Figure 4.2.4 shows the morphology for the damage above the damage threshold for a single 532 nm laser pulse at 3.68 mJ (15.5 GW/cm^2). A typical cylindrical damage pattern accompanied by breakdown paths can be seen from this figure. These breakdown paths are usually oriented along a definite crystalline directions.[67, 68] The breakdown paths do not depend on the orientation of the crystal relative to the polarisation of the electric field and lie within the reflection plane. Thus, the operating mechanism of laser damage appears to be a dielectric breakdown.[69] It was reported earlier that the damage pattern in ZTS reflects the mirror symmetry of the plane of damage and the dominant cause for the damage is dielectric breakdown with the damage propagating as stress
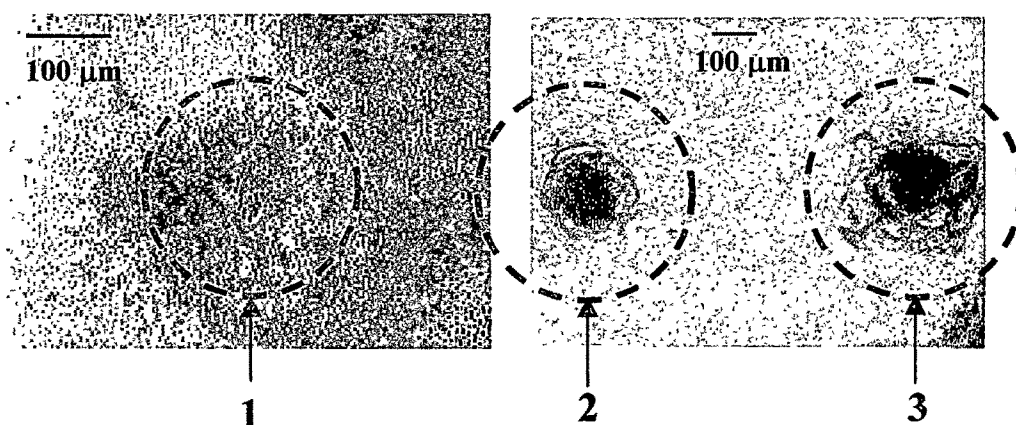
150

Figure 4.2.3. Laser damage patters at 532 nm for 500 laser shots at different peak pulse intensities (1-0.43 GW/cm^2, 2-1.36 GW/cm^2 and 3-1.75 GW/cm^2)

fractures. Fig.4.2.4 shows that the breakdown paths are parallel to [012], which is the hardest direction of ZTS crystal.[70] This indicates that there is a strong correlation of laser damage at 532 nm with the mechanical hardness anisotropy.[71] Fig. 4.2.4 also shows a breakdown path along c-direction ([001] direction) of the ZTS crystal.

Figure 4.2.5 shows the dependence of the laser damage threshold at 532 nm on the number of pulses (at 10 Hz repetition rate) causing laser damage. As expected, the highest intensity is required to induce laser damage with a single shot. This required intensity reduces with increasing number of pulses and tends to saturate at a certain value, which in this case is around 0.08 mJ (0.34 GW/cm^2). Note that the graph in Fig. 4.2.5 is plotted on a logarithm scale and therefore does not appear to saturate. Thus for applications requiring long-term exposure to ~8 ns pulses at 10 Hz repetition rate, one can assume that the absolute damage threshold at 532 nm to be ~ 0.34 GW/cm^2.

Determination of exact laser damage threshold at 1064 nm has been difficult. For a single ~10 ns shot, the ZTS crystals withstand laser damage at intensities estimated up to 50 GW/cm^2 (4.24 mJ). For the same pulse energy but for 10 shots at 10 Hz repetition rate, the sample shows distinct signs of laser ablation as can be seen from the pattern shown in Fig. 4.2.6. Such a laser ablation is not observed in earlier studies reported by V. Venkataramanan *et al.*[66] It should be noted that their work was performed with ~ 40 ps pulses at 10 Hz repetition rate and where thermal effects are more pronounced than in the nanosecond regime. Therefore for irradiation of the ZTS sample with picosecond pulses at 1064 nm, the presence of the N-H vibrational overtone absorption at 1040 nm does not result in increased local temperature. In the present work using ~ 10 ns pulses at 1064 nm, the N-H overtone around 1040 nm
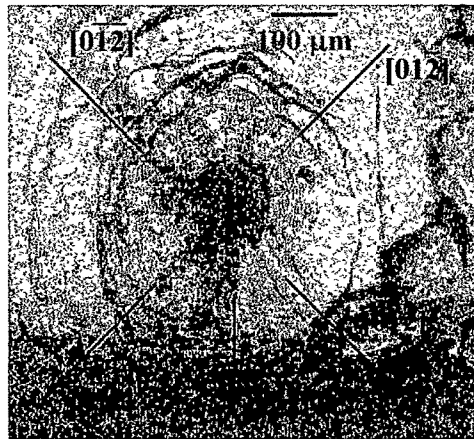
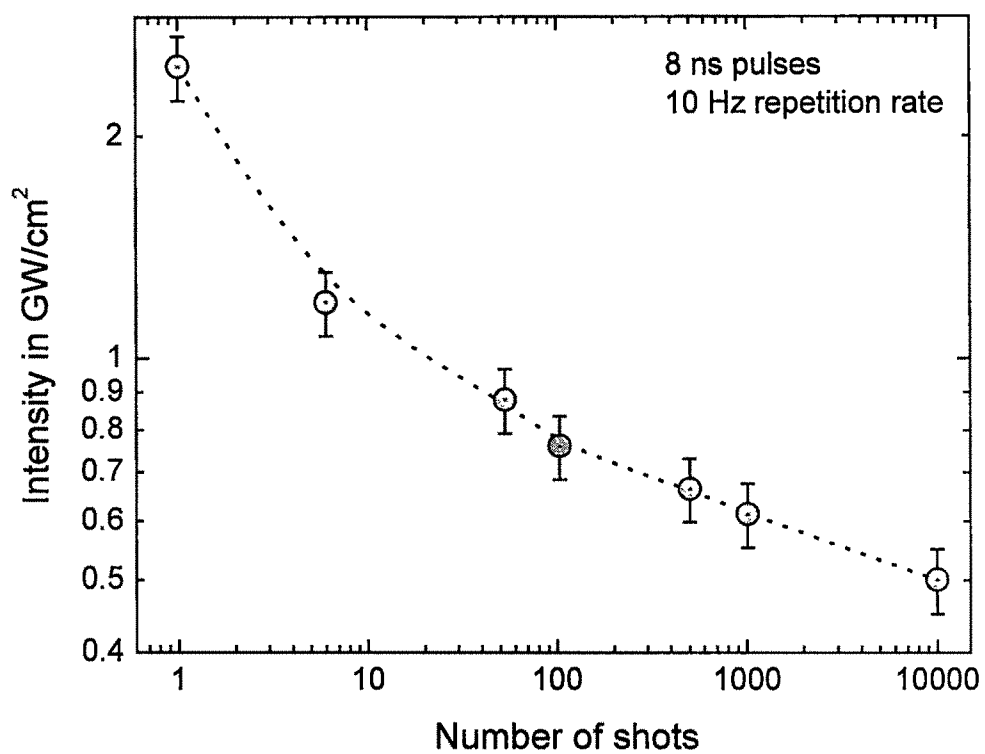**Figure 4.2.4.** Laser damage pattern at 532 nm for single shot at 15.5 GW/cm^2.

Figure 4.2.5. Laser damage is shown as a function of number of laser shots from the 10 Hz, 10 ns Nd: YAG laser.
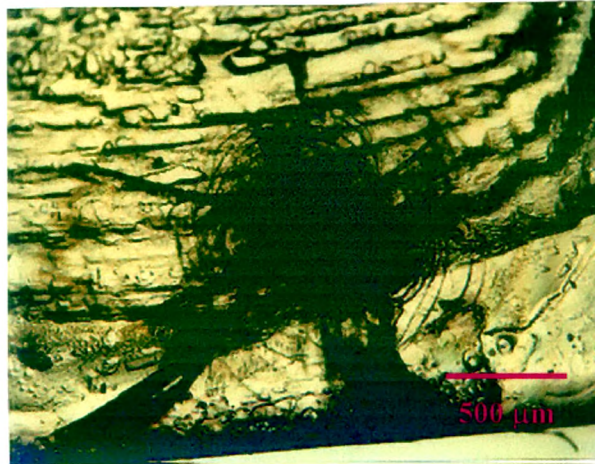
154

Figure 4.2.6. Laser damage profile resulting from ~8 ns pulses at 1064 nm at 50 GW/cm^2. The irregular spots (other than the striations) seen in this picture well beyond the dark irradiation area is expected to be a result of redeposition of ablated material.

may lead increased local temperature at the focused spot. This could explain the ablation behaviour. Thermal effects need to be considered for pulse widths that are nanoseconds and slower and for higher repetition rates where cumulative thermal effects become important. The effects of thermal lensing are described in this thesis (section 4.3.3).

4.2.3.3. Factors Affecting laser damage on ZTS crystals:

As explained in section 4.2.2.3, several factors need to be carefully considered to determine the true laser damage thresholds. Of particular importance are the spatial and temporal characteristics of the laser pulse. In addition the "quality" of the surface also affects the laser damage threshold. First, the laser that was used for the damage studies described above has beam diameter of 5.5 mm. The beam from the unseeded Nd:YAG laser is not a TEM_{00} Gaussian profile. It is slightly elliptical (5.0 mm < diameter < 6.0 mm) with some non-uniformities in its profile. This results in higher intensity "hot spots" that could result in damage threshold estimate that is lower than the actual value. Second, the temporal profile of the laser pulses is nearly "top-hat." A Gaussian or a Lorentzian temporal profile delivers higher peak powers to the sample than the existing pulse shape. This factor was taken in to account while calculating the intensities corresponding to the incident pulse energies. Third, the ZTS crystals were used for damage studies in an as-grown state. The surface was not polished or antireflection-coated. On many samples in ZTS, the cleaved (100) surfaces show the presence of striations or steps, which could lower the damage threshold. Thus, it can be concluded that the damage threshold values reported in this work are conservative estimates and that the ZTS crystals can withstand impact of laser intensities at least up to intensities reported in this thesis.

4.2.4. Conclusions

The detailed laser damage study on the ZTS crystal with 10 ns pulses at 532 nm and 10 Hz repetition rate is described for the first time in this thesis. Prominent cracks appear along [012] and explain the mirror symmetry of the crystal. Damage thresholds were determined for varying number of shots from single shot upto 10,000. Single shot damage occurred at an intensity of 50 GW/cm^2. This laser damage intensity saturates at 0.34 GW/cm^2 as the number of shots reach 10,000.

REFERENCES:

1. J. A. Armstrong, N. Bloembergen, J. Duccing, and P.S.Pershan, *"Interactions between Light Waves in a Nonlinear Dielectric,"* Phys. Rev., **127**, (1962)

2. J. P. Basrur, F. S. Chao, P. L. Liu, J. Sipior, G. Rao, G. M. Carter, and Y. J. Chen, *"The process and efficiency of Ultraviolet generation from gallium nitride blue emitting diodes,"* Appl. Phys. Lett. **71** (10), 1385, (1997).

3. H. Jones-Bey, "Researchers find high-power, "Laser Focus World, Vol. **34**, No.11, 15-16 (1998).

4. J. Wejorn, and R. Waarts, *"Frequency doubling offers advantages for blue lasers,"* Laser Focus World, Vol. **34**, No.5, (1998).

5. F. C. Zumsteg, J. D. Bierlein, and T. E. Gier, *"KxRb1-x TiOPO4; A new nonlinear optical material,"* J. Appl. Phy. **47**, 4980 (1976).

6. S. Singh in *"Handbook of Lasers"*, Chemical Rubber Company, Clevland, Ohio, 1971.

7. C. Chen, B. Wu, A. Jiang, G. You, *"A new type of ultraviolet SHG crystal b-BaB₂O₄,"* Sci. Sinica (series B) **28**, 235 (1985).

8. Shinotsuka, M., Onagi, N. and Harigaya, M., Jap. J. App. Phys. **39**, 976 (1999)

9. Bringans, R. D., Mat. Res. Soc. Proceedings **482**, 1203 (1998)

10. Gustafsson, U., Somesfalean, G., Alnis, J., Svanberg, S., Appl. Opt. **39**, 3774 (2000)

11. Tamosaitis, R., Melikechi, N., Laser focus world. **34**, 159 (1998)

12. Hecht, J., Laser focus world. **29**, 67 (1993)

13. Cunningham, R., Lasers & Optronics **13**, (1994)

14. See, for example, *Compact Blue-Green Lasers*, OSA Technical Digest Series **6** (Optical Society of America, Washington, DC, 1992)

15. Risk,W. P., Opt. Photon. News **1**, 10 (1990)

16. R. Boyd, *"Nonlinear Optics"*, 1st Ed., Academic Press (1992)

17. J. A. Armstrong, N. Bloemgregen, J. Duccing, and P.S.Pershan, *"Interactions between Light Waves in a Nonlinear Dielectric*, "Phys. Rev., **127**, (1962)

18. C. Wang and G.Racette, Appl. Phys. Lett. **6**, 169 (1965)

19. J. A. Giordmanie and R. C. Miller, Phys. Rev Lett, *"Tunable coherent parametric oscillation in LiNbO₃ at optical frequencies,"* **14**, 973 (1965)

20. P. Franken and J. Ward, Rev Mod. Phys.**35**, 23(1963)

21. R. Terhune, P. Maker and C. Savage, Phys. Rev. Lett , **8**, 404 (1962)

22. R. Minch, R. Terhune and C. wang, Appl Opt. **5**, 1595 (1966)

23. W. Kaiser and C. Gerrett, Phys. Rev. Lett, **7**, 229, (1961)

24. G. Eckhart, Phys. Rev Lett **9**, 455 (1962)

25. R. Chiao, C. Townes and B. Stoicheff, Phys. Rev. Lett, **12**, 592 (1964)

26. D. Mach, V. Morozov, V. Starunov and I. Fabelinskii, JETP Lett., **2**, 22 (1965)

27. L. Mandel and E. Wolf, *"Optical Coherence and Quantum Optics,"* Cambridge Press, 1070 (1995)

28. E. Sauter, "Nonlinear Optics," Wiley (1996)

29. Giordmaine, J. A., *"Mixing of light beams in crystals,"* Phys. Rev. Lett. **8**, 19-20 (1962)

30. Maker, P. D., Terhune, R. W., Nssenoff, M and Savage, C. M., *"Effects of dispersion and focusing on the production of optical harmonics,"* Phys. Rev. lett. **8**, 21 (1962).

31. A. Yariv, "*Quantum electronics*," 3rd edition, John Wiley and Sons, (1988).

32. Born, M. and Wolf, E Principles of Optics, Pergamon, Oxford (1959)

33. E. E. Wahlstrom, "*Optical Crystallography*," John Wiley & Sons, New York (1943)

34. F. Zernike and J.E.Midwinter, "*Applied Nonlinear Optics*", Wiley, New York (1973)

35. S. Singh, "*Handbook of Laser Science and technology*", (edited by M. J. Weber), Vol. III: Part 1, Sect. 1.1, CRC Press (1986)

36. G.D. Andreeti, L, Cavalca and A. Musatti, Acta Crystal. **B24**, 683-690 (1968)

37. G. C. Catella, J. H. Bohn, D. A. Roberts and W. R. Cook, SPIE **1104**, 66 (1989).

38. P. R. Newman, L. F. Warren *et al.* Mat. Res. Soc. Symp. Proc. Vol. **173** (1990).

39. H. O. Marcy *et al* Applied Optics, Vol.**31**, No.24 (1992).

40. D. Eimerl, "*Electro-optics, linear, and nolinear optical properties of KDP and its isomorphs,*" Ferroelectrics **72**, 95-139 (1987).

41. Uma B. Rambadran, Angela L. McPherson, and David E. Zelmon, J. Appl. Phys. **76** (2), (1994).

42. H.O. Marcy, L. F. Warren *et al.* Mat. Res. Soc. Symp. Proc. Vol. 228 (1992).

43. V. Venkataramanan, C. K. Subramanian, and H. L. Bhat, J. Appl. Phys. **77** (11), (1998).

44. H. O. Marcy, L. F. Warren, M. S. Webb *et al.* CThR**21**, CLEO '91 Digest (IEEE)

45. R. W. Munn and C. N. Ironside, "*Principles and Applications of Nonlinear Optical Materials*" 1st edition Chapman and Hall, Published by Blackie Academic & Professional, 1993.

46. Guliano, C. R. Appl. Phys. Lett. , **5**, 137 (1964).

47. Cullom, G. H. , Waynant, R. W. Appl. Opt. **3**, 989 (1964).

48. *"Laser Damage in Optical Materials "* by Roger Wood, Bristol; Boston: Hilger 1986.

49. R. W. Whitworth, Adv. Phys. **24**, 203 (1975), M. V. Galustashvili and D. G. Driyaev, Fiz. Tverd. Tela (Leningrad) **25**, 1904 (1983) [Sov. Phys. Solid State 25, 1101 (1983)]

50. Bolembergen N. Appl. Opt. **12** 661,1973.

51. Martinelli J 1966, J. Appl. Phys. **37** 1939, Hopper R W, Lee C and Uhlmann D R, NBS Special Publication **341,** 55,(1970).

52. Davit J, NBS special publication **341,** 37 (1970).

53. Sparks NBS special publication **435,**331,1975.

54. Zerev, G. M., Mikhailova, G. N., Pashkov, V. A., Soloview N. M. Siviet JETP, **53,** 1849 (1967)

55. Molchanov, A. G. Physika Tverdogo Tela **12,** 954 (1970), Epifanov, A. S., IEEE J. Quant. Electr. **QE-17,** 2018 (1981)

56. Manenkov A A, Matyushin G A, Nechitailo B S, Prokhorova A M and Tsaprilov A A NBS special publication **669** ,436,1982.

57. Lee C S, Koumvakalis N and Bass M, NBS publication **699,** 186,1982.

58. Merkic L, Bass M and Swimm R T NBS Special Publication **669,** 50, 1982.

59. Wood R M, Waite P and Sharma S K, Second General Conference of the Condensed Matter Division of the European Physical Society (Manchestor), Europhysics Conference Abstracts Vol.**6A,** 396, (1982).

60. Wood R M, Waite P and Sharma S K, NBS Special Publication **669,** 33, (1982).

61. Porteus J O, Faith W N and Allen S D, NBS Special Publication **638,** 273, (1981).

62. Lewis K L and Savage J A, NBS Special publication **688,** 227, (1983).

63. Lunt D, NBS, Special Publication **688,** 287, (1983).

64. Partlow and Heberlein J V R, NBS special Publication **688**, 417,(1983).

65. Guenther K H *et al.* Appl. Opt. **23** (2b) 3743,1(984).

66. V. Venkataramanan, *et al.* J. Appl. Phys, **77** (11), June (1995).

67. F. Seitz, Phys. Rev. **76** 1376, (1949).

68. J. W. Davission, Phy. Rev **70** 1376 (1946).

69. R. J. Bolt, Optics Communication **100** , 399, (1993).

70. S. S. Gupte and C. F. Desai, Cryst. Res. Tech, **34** 1329, (1999).

71. V. Venkataramanan, G. Dhanaraj, Ferroelectrics, Vol. **155**,13,1994.

PART B: Other Optical Characterisation

4.3. Other Optical Characterisations

4.3.1. Introduction

The theoretical and experimental investigations of optical behaviour of solids deal primarily with optical reflection, transmission and absorption properties and their relation to the optical constants of the bulk and thin films. The absorption studies have led to an understanding of a variety of interesting phenomena, which have thrown considerable light on the electronic structure of solids. For absorption studies, photons of selected wavelength are directed at the sample and their relative transmission/absorption is observed. For a non-linear optical crystal, the absorption at the operating wavelengths can significantly alter its performance. Characterisation of its absorption, which is often small, is therefore necessary. In addition absorption studies provide the most direct and the simplest method for determining the band structure of the crystal.

When a low intensity light beam passes through a transparent substrate or falls on a reflecting mirror or on an absorbing medium, little or no effect may be observed. This is the realm of linear optics and is part of our everyday experience As the intensity of the beam increases a whole range of reversible interactions may become obvious. These include strain, distortion, expansion, temperature rise, non-linear transmittance and absorption, electro-optic effects, and self-focusing. Typically, only lasers have sufficient

intensity to alter the optical properties of materials. At high intensities the refractive index n becomes dependent on the intensity/energy incident on the sample.

For non-linear optical studies an obvious requirement is that the material be transparent at the wavelengths of interest. A wide transmission range for the material is often desirable, as it extends the useful frequency range of the device. The crystal must also exhibit low optical losses at the frequencies involved. These loses may take the form of absorption or scattering losses or both. Low losses are very important as high losses can severely affect the conversion efficiency of the non-linear process or the threshold for oscillation in parametric devices. Moreover, absorption losses can give rise to thermal distortions in the material, which drastically limit device performance, particularly at high power levels, and lead to premature optical damage.

In section 4.3.2 the author discusses the linear absorption studies undertaken for the ZTS crystal.

4.3.2. Optical Absorption Studies

As described above optical absorption spectra reveal valuable information about the material under investigation. In the following sections results of absorption measurements are described. Absorption studies were carried out in two wavelength regions. First the absorption spectra from the near-ultraviolet (UV) to the near-infrared wavelengths (NIR) were determined. This was done to assess the transparency of the crystals in the wavelength range of application. In pH studies, described in Chapter 2, the absorption spectra in this wavelength range were used to characterise the quality of the crystal as a function of the growth solution pH. The details of this experiment are also

discussed in this chapter. In addition, absorption data was used to determine the band gap of the crystal. Second, the absorption spectrum for these crystals was measured in the mid-infrared region using FTIR spectroscopy. These results are in good agreement with earlier structural studies based on FTIR spectroscopy reported by other authors.[1, 2]

4.3.2.1.Experimental set-ups

An FTIR spectrophotometer (BOMEM MB-104) with a resolution of 4 cm^{-1} was used for the IR optical measurements. Freshly cleaved thin crystals having thickness about 0.5 to 1 mm were mounted on the sample holder side. The absorption spectrum was recorded in the wave number range of 510 cm^{-1} to 4000 cm^{-1} (wavelength from 10.6 μm to 2.5 μm).

An UV spectrometer (*Perkin-Elmer*) with a resolution of 3 nm was used to obtain the absorption spectra of a freshly cleaved ZTS crystal having thickness about 0.5 to 1mm. The optical absorption was measured in the wavelength range 190 to 400 nm. By analysing the spectrum, absorption coefficient was calculated as a function of photon energy. A Cary 100 UV/VIS spectrometer with a resolution of ~ 1 nm was used to obtain the absorption spectra of crystals from different pH growth solution discussed in chapter 1. The absorption coefficient was determined from these absorption spectra.

4.3.2.2. Infrared (IR) Absorption Studies

Figure 4.3.1 is an IR spectrum for the ZTS crystal grown by the author. Within the experimental resolution, the exhibited bands matched with the earlier reported assignments on the IR characterisation of the ZTS crystal.[1,2] The thiourea crystal exhibits the bands in the region 400-750 cm^{-1}, 1050-1150 cm^{-1} and 1300-1650 cm^{-1}. The vibrational frequency shifts and appearance of additional frequencies (metal-sulphur) observed in the FTIR spectrum of ZTS establish that the Zn^{+2} ions are co-ordinated with the thiourea group.[1] In a detailed work by S. Selvasekarapandian and co-workers, the prominent vibrational lines observed at 740 cm^{-1} and 1471 cm^{-1} in FTIR spectra are attributed to the C-N symmetric and asymmetric stretching vibrational modes, respectively. The strong FTIR peaks observed at 1089 cm^{-1} and 1472 cm^{-1} have been assigned to the symmetric and asymmetric stretching vibrational mode of C=S, respectively. Absorption peaks in the high wavenumber region (3100-3400 cm^{-1}) arises due to the N-H stretching vibrations. The absorption around 4000 cm^{-1} (2500 nm) can be attributed to the symmetric and asymmetric vibrations of NH_2 groups.[3]
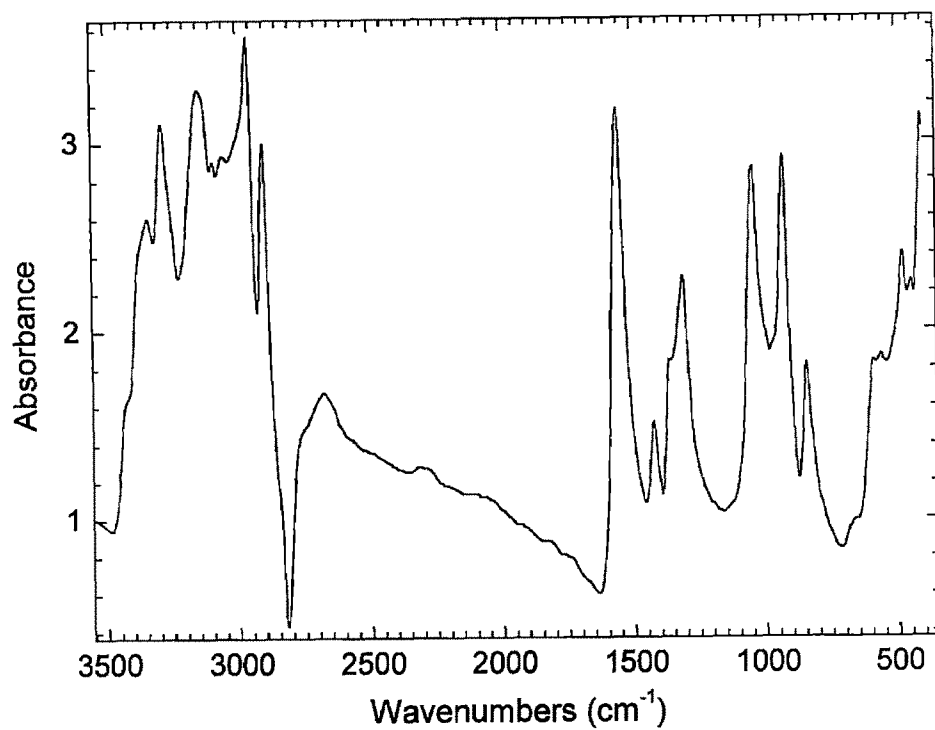
166

Figure 4.3.1. IR spectrum of ZTS crystal

4.3.2.3. Band gap for bulk ZTS crystal

When a beam of photons with energy $h\nu > E_g$ (E_g is the bandgap) falls on an absorbing material, as shown in figure 4.3.2, there will be some predictable amount of absorption determination by properties of the material. The ratio of transmitted to incident light intensity depends on the photon wavelength and the thickness of the sample.

The intensity of light transmitted through the sample with thickness t is

$$I = I_0\, e^{-\alpha\, t} \qquad\qquad 4.3.1$$

where α is the absorption coefficient, I_0 is the incident photon beam intensity and I is the transmitted intensity.

Near the absorption edge, the absorption coefficient is expressed as

$$\alpha \sim \left(h\nu - E_g\right)^{\gamma} \qquad\qquad 4.3.2$$

where $h\nu$ is the photon energy. E_g is the optical gap, γ is a constant, which is equal to 1/2 and 3/2 for allowed direct transition and forbidden direct transition. In addition γ equals 1/2 for allowed indirect transitions to exciton states where an exciton is a bound electron-hole pair with energy levels in the band gap and moving through the crystal lattice as a unit.

The absorption coefficient is expressed in terms of a coefficient, which is defined as the relative rate of decrease in light intensity L (hv) along its propagation.

$$\alpha\left(h\nu\right) = \frac{1}{L\left(h\nu\right)} * \frac{dL\left(h\nu\right)}{dx} \qquad\qquad 4.3.3$$

Figure 4.3.2. Optical absorption of a photon with energy $h\nu >$ the bandgap E_g.

where $L(hv)$ is incident light intensity, α is the absorption coefficient.[4, 5] For direct transitions, the absorption coefficient relates to the photon energy as

$$(\alpha h v) = B(h v - E_g)^x \qquad 4.3.4$$

where x = ½ for allowed transitions and x = 3/2 for forbidden transitions; E_g is the direct energy gap and B is a parameter that depends on the transitions probability.

For indirect transitions,

$$(\alpha h v) = A(h v - E_g \pm E_p)^x \qquad 4.3.5$$

where x = 2 for indirect allowed transitions and x = 3 for forbidden transitions. E_g is the band gap and E_p is the absorbed or emitted phonon energy.[6, 7, 8] At room temperature, transitions, both with phonon emission and phonon absorption, will contribute to the absorption.

Figure 4.3.3 is the UV spectra for ZTS crystal. From this spectrum the plots of $(\alpha h v)^{1/2}$ vs hv and $(\alpha h v)^2$ vs hv were obtained.

Further these plots of $(\alpha h v)^{1/2}$ versus hv and $(\alpha h v)^2$ versus hv were used to evaluate the optical band gaps. The plot of $(\alpha h v)^2$ versus hv for ZTS crystal is shown in Fig 4.3.4. The plot is observed to be linear giving the band gap, as the intercept on the hv axis, to be 3.0 eV, in agreement with the value reported by Marcy *et al.*[9]
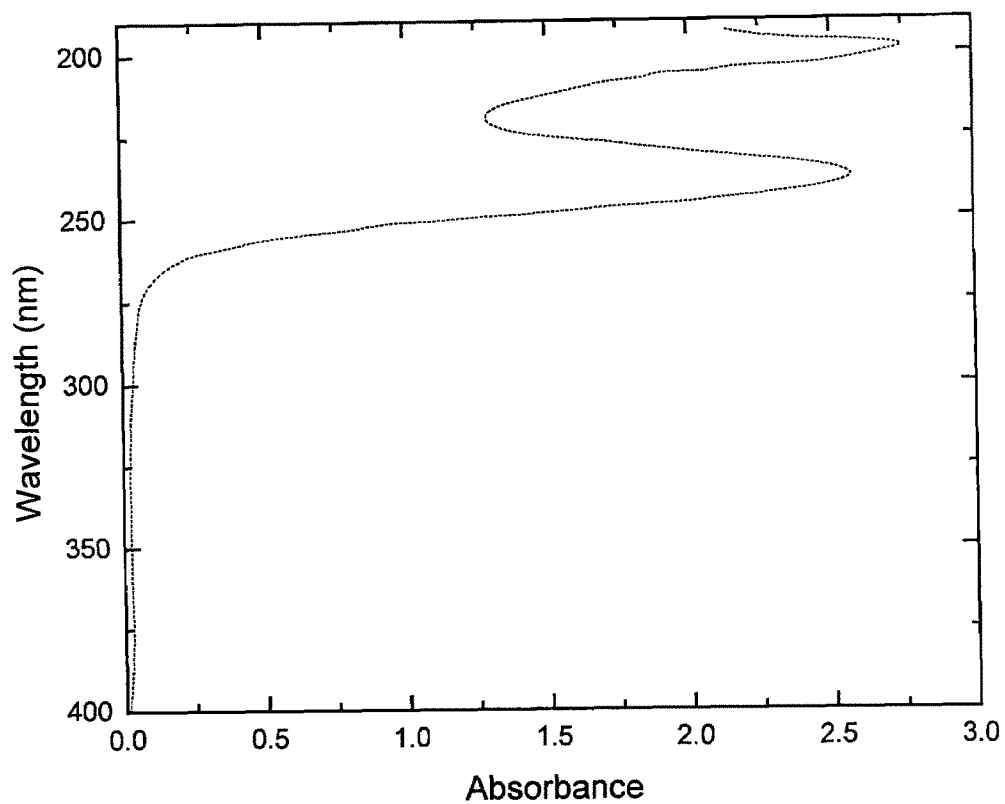
170

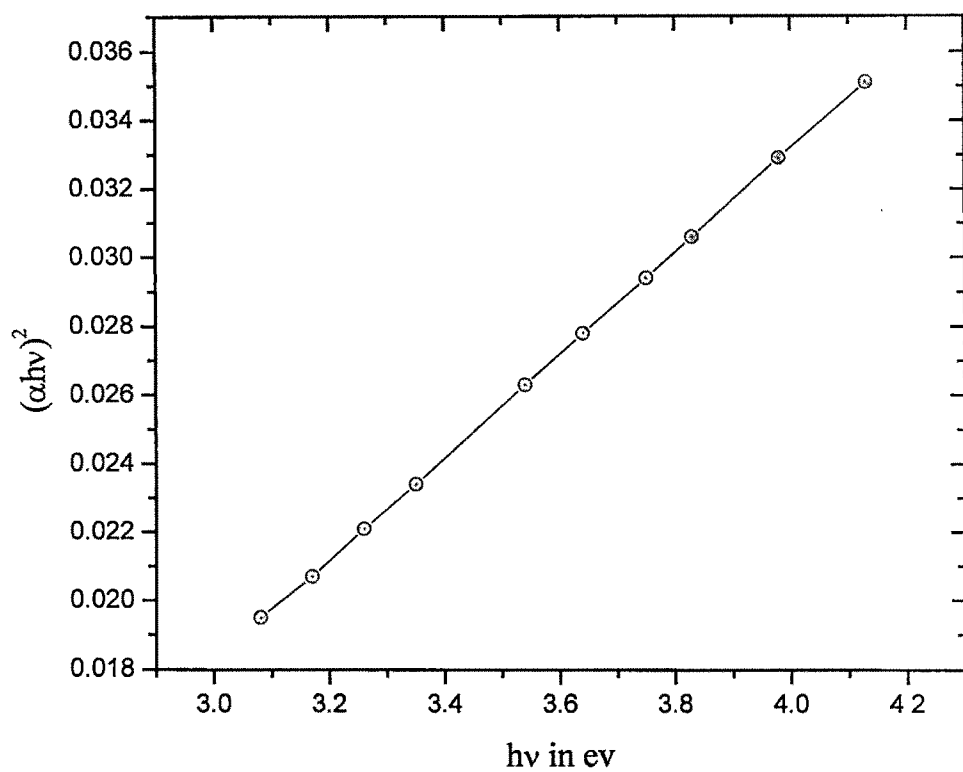**Figure 4.3.3** The UV absorbance spectra for ZTS.

171

Figure 4.3.4. The plot of $(\alpha h\nu)^2$ vs $h\nu$ for ZTS

4.3.2.4. Quality of crystals using optical transmission

pH studies:

A previous study reports on the influence of pH on the growth morphology of ZTS crystals, with the pH value ranging from 3.15 to 6.54.[10, 11] Lower pH was reported to be preferable for better crystals, where uniform growth along all crystal direction was assumed to be signature of better crystals. This study investigates the influence of pH in the range 2.5 to 4.2, using the optical absorption coefficient and dislocation density (discussed in Chapter 1) as direct measures of crystal quality. The transmission spectra of the crystals obtained from solutions of different pH values were obtained using a Cary 100 UV/VIS spectrophotometer and absorption coefficients were calculated. Figure 4.3.5 shows the variation of the absorption coefficient as a function pH. The absorption coefficient at 500 nm (visible) and 320 nm (UV) is shown as a function of pH. The absorption coefficient is minimum for crystals grown from solutions within the 3.5-3.8 pH range. This suggests that the crystals from pH 3.6 are of better quality and of higher transparency. The variation of the absorption coefficient with solution pH closely follows the variation of the growth rate per unit mass with solution pH. Since the highest transparency or lowest absorption coefficient is desired, the optimum solution pH is the one that yields the lowest growth rate. This suggests that the lower growth rate at pH ~ 3.5 facilitates favourable rearrangement at the molecular level yielding single crystals of better quality.
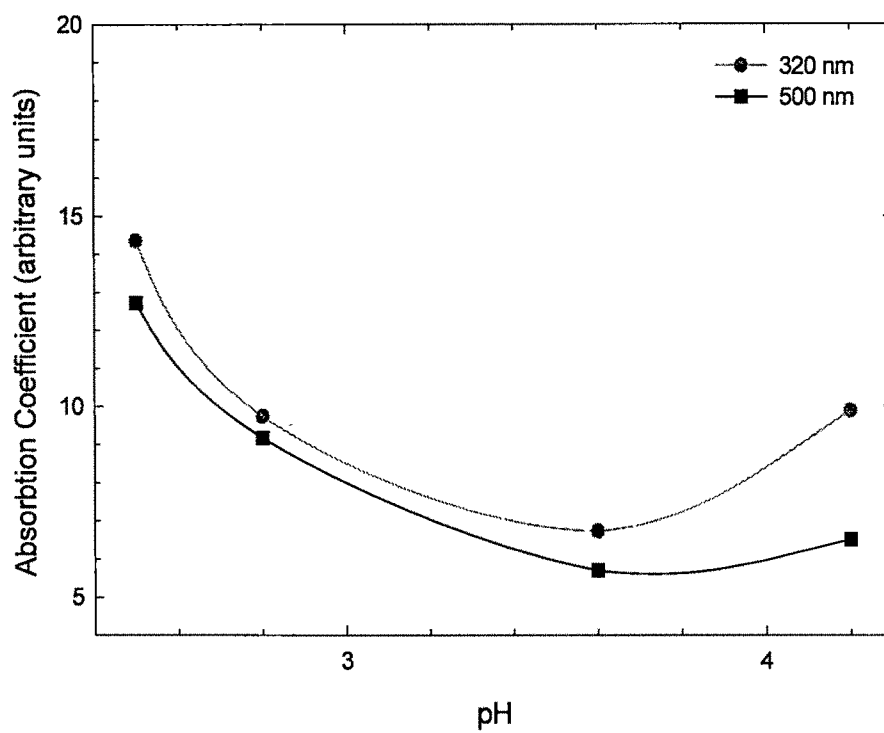
Figure 4.3.5. The variation of the absorption coefficient is shown as a function of growth solution pH for wavelengths at 500 nm (squares) and 320 nm (circles).

4.3.3. Thermal Lensing Spectroscopy

One important issue of a non-linear optical crystal is the characterization of the absorption in the spectral region of the fundamental source. For many non-linear optical (NLO) applications, even a small absorption can severely degrade the performance of the NLO device. This is particularly true if the NLO crystal is used inside the laser cavity. Due to the absorption being small, high sensitivity methods must be used for such characterisation.

In recent years a number of thermo-optical spectroscopy techniques have been suggested especially for measuring weak absorption of solutions. These techniques include thermal lensing,[12, 13, 14] interferometry,[15, 16, 17, 18] photo thermal beam deflection,[19] photo thermal radiometry,[20, 21] and photo acoustic spectroscopy.[22] Using solutions with low background absorption, absorptives ranging from 10^{-5} to 10^{-7} cm^{-1}, have been measured with interferometry[15, 23] and thermal lensing.[14, 24]

Thermal lensing spectroscopy[25, 26, 27] and its variations such as Z-scan[28, 29, 30] are high sensitivity techniques that have been applied in gases[31, 32] liquids[33, 34] and solids[35, 36] for characterization of samples with small absorption. However, until now these techniques have not been applied for the characterization of absorption in second harmonic crystals. The most widely used method for the measurement of absorption in nonlinear crystal is the calorimetric method developed by Johnson[37] and Barnes and coworkers[38] as an extension of the ideas of Rich and Pinnow.[39] In this method, a direct measurement of the surface temperature of the crystal is performed. The crystal must have a particular shape

for the correct interpretation of the experimental results. In the TL technique there is no need for recording the crystal temperature, since the signal is a direct measurement of the absorption, thereby avoiding difficulties in the interpretation of the results. There are no restrictions for the shape and dimensions of the crystal. Furthermore, the use of reference materials simplifies its implementation. Finally, a pump-probe TL experiment allows the measurement of the absorption spectrum of the crystal without the concern of scattering and reflection losses. In this section the author demonstrates, the use of a pump-probe thermal lens and Z-Scan experiments for the measurement of the NIR spectrum and the absolute value of the absorption coefficient of ZTS.

4.3.3.1. Concept of thermal lensing and Z-scan techniques

With increasing intensity or energy of light incident on the sample the refractive index of the material is no longer constant but changes with the exact irradiation conditions. Under such circumstances the refractive index seen by the laser beam passing through the sample can be expressed as

$$n = n_o + \int_0^\tau n_{NL}(t)I(t)\,dt \qquad\qquad 4.3.6$$

where n_0 is linear refractive index, $I(t)$ is the instantaneous intensity of light and n_{NL} is a measure of the non-linear response of the medium and is called the non-linear index of refraction. For the non-linear response of the medium originating from fast non-linearities that are electronic in origin, the non-linear response can be expressed as

$$n_{NL}(t) = n_2\,\delta(t) \qquad\qquad 4.3.7$$

However, for time scales typically longer than a few hundred picoseconds thermal effects become prevalent and depend on the cumulative accumulation of energy absorbed by the medium. The thermal contribution to the non-linear refractive index can be expressed as

$$n_{NL}(t) = n_{TH} \qquad\qquad 4.3.8$$

For cases where the thermal effects dominate, the dependence of the refractive index on the energy of the incident light can be written as

$$n = n_o + n_{TH} \int_0^\tau I(t)\,dt \qquad\qquad 4.3.9$$

The incident light that is absorbed in the sample generates an inhomogeneous distribution of the temperature in the interaction volume. The thermal diffusion equilibrates the amount of heat injected by the absorption process. At the equilibrium of these two processes, a stationary thermal lens is generated in the medium. The presence of the thermal lens alters the propagation of the beam along the sample and distortions of the beam profile are observed at the far field.

A method based on thermal lensing is the Z-scan method used for detecting optical non-linearities. This method provides a highly sensitive means of detecting nonlinear refraction and nonlinear absorption. In the Z-scan technique a thin sample is scanned through a focus of an intense laser beam with a Gaussian spatial intensity profile. This is illustrated in the figure 4.3.7. The output from the sample is monitored by a detector, which is placed behind a pinhole. The intense beam induces both absorption and refraction non-linearities. For the refractive non-linearity, a Gaussian laser beam induces a non-uniform refractive index in the sample. This non-uniform refractive index can be interpreted as a lens that affects the beam propagation. The nature of the lens depends on

177

the sign of n_2 If $n_2 > 0$, there is a positive lens and self-focusing and if $n_2 > 0$, a negative n_2 leads to a negative lens and self-defocusing as shown in figure 4.3.6.

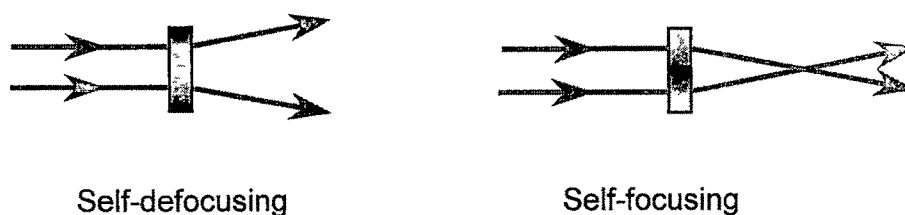Self-defocusing   Self-focusing

Figure 4.3.6. Concept of thermal lensing

To understand how the Z- Scan technique works, consider the sample starting between the focal point and the lens (as illustrated in the figure 4.3.7). When the sample is far from the focus there is low intensity and negligible nonlinear refraction occurs; therefore the transmittance observed through the pinhole is constant. As the sample approaches the focus the intensity increases leading to self-lensing in the sample. A negative self-lensing prior to the focus will tends to collimate the beam resulting in a beam narrowing at the aperture, which results in an increase in the intensity on the detector. As the scan continues and the sample passes through the focus into the post-focus region, the negative lensing effect will tend to increase the beam divergence, resulting in a beam broadening at the aperture and less light reaching the detector. For a positive non-linearity and positive lensing effect, the light on the detector decreases when the sample is in the pre-focus region and increases when the sample is in the post-focal region --- the opposite behaviour results from the negative lensing effect. The Z-scan is simple, straightforward measuring techniques
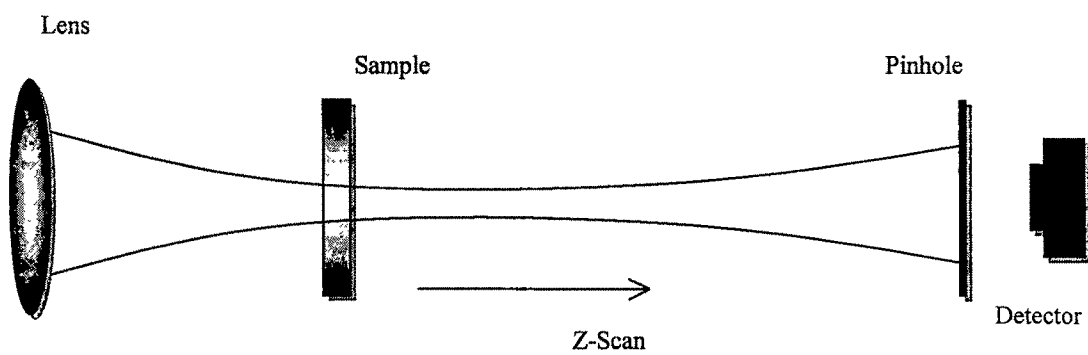
178

Figure 4.3.7. Z-scan technique

that yield accurate values for the nonlinear optical coefficients. There is no time information about the non-linearity, and therefore it does not distinguish between different mechanisms; in particular, it does not separate out thermal effects. In the Z-scan technique, a collimated laser beam is focused with a lens while keeping the input power constant. The sample is translated through the focal plane of the lens while monitoring the far-field transmission through an aperture. A normalized transmission is defined to be the ratio of the far-field transmission over the linear transmission (the sample far away from focus). By plotting the normalized transmission against the sample position, a dispersion shaped curve is obtained from which the sign as well as the magnitude of the nonlinear refraction coefficient can be easily obtained. A schematic diagram of a typical Z-Scan curve is shown in figure 4.3.8. The aperture transmission shows a typical peak-
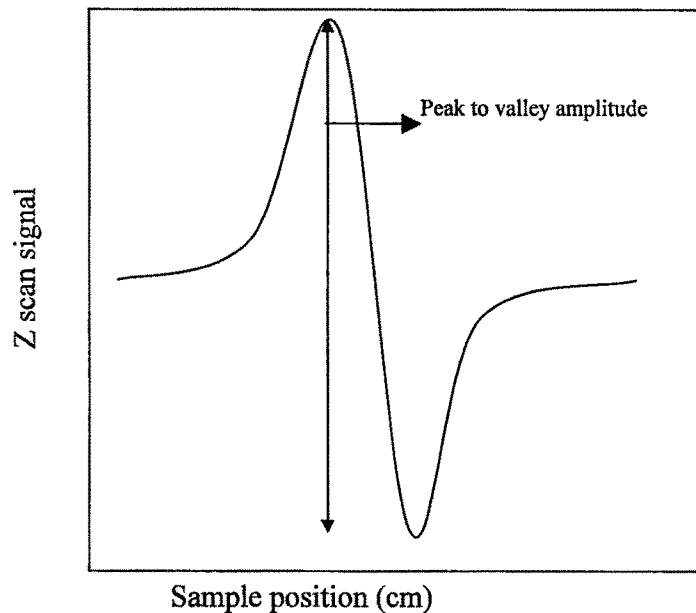

Figure 4.3.8. Schematic diagram of Z-Scan Curve.

valley transmission dependence on the sample position Z. The magnitude of the peak-valley amplitude is a measurement of the sample nonlinear refraction. The shape of the dispersion shaped curve is affected by many factors, such as the spatial beam quality, sample thickness, anisotropy of the nonlinear refractive index, high reflectivity, and other nonlinear processes like two-photon absorption and free-carrier absorption. A purely weak refractive nonlinearity yields a dispersion shaped curve that is symmetric about the focus. As mentioned earlier, thermal non-linearities can be detected by Z-Scan methods as the thermal effects leads to a nonlinear refraction. This is usually because the refractive index is a function of temperature, $\Delta n = \left(\dfrac{\partial n}{\partial T}\right)\Delta T$.

A variation of this technique uses two beams. One beam, called the pump, is used to create the thermal lens. The second beam, referred to as the probe beam, is used to monitor the thermal lens. This idea has important spectroscopic applications. If the pump beam is tuneable, the aperture transmission of the probe beam at a fixed wavelength yields the required spectral signature (photo thermal absorption spectrum). Thermal lensing Z-scan experiment is complementary to the thermal lensing spectroscopy. By keeping the pump field wavelength fixed, one measures the probe field aperture transmission by scanning the sample in the longitudinal direction around the pump field focal point. This is shown in figure 4.3.9. The probe field aperture transmission is measured as a function the Z-position and yields a typical peak-valley transmission dependence on the sample position. The magnitude of the peak-valley amplitude is a measure of the sample nonlinear refraction.
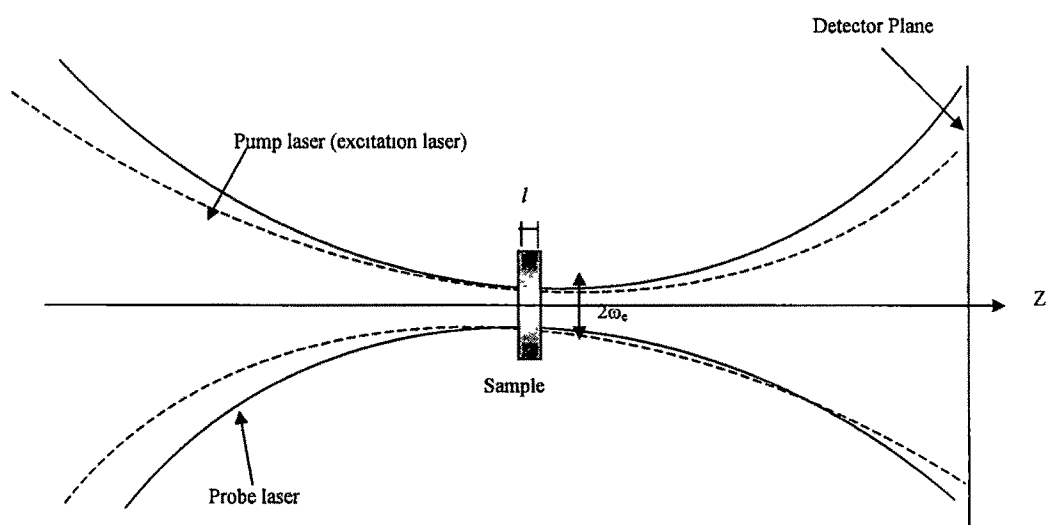
181

Figure 4.3.9 Scheme of the geometric position of the beams in a mode-matched dual-beam thermal lens experiment

In the situation of a thermal lens experiment, the peak-valley amplitude of the Z-Scan signal measures the absolute magnitude of the absorption coefficient. The effect of the thermal lens on the probe beam can be formulated as an additional phase shift Φ with respect to radial position and time and can be expressed as [40]

$$\Phi(r,t) = \frac{\theta}{2} \int\limits_{\frac{1}{1+\frac{2t}{t_c}}}^{1} \left[1 - \exp\left(-2 \, \tau r_1^2 \Big/ \omega_e^2 \right) \right] \frac{d\tau}{\tau}, \qquad 4.3.10$$

where

$$t_c = \omega_e^2 \Big/ (4D) \qquad 4.3.11$$

is a characteristic thermal time constant associated with thermal diffusion in the sample, D is the thermal diffusivity of the sample, ω_e is the radius of the excitation beam in the sample;

$$\theta = -\frac{P_e A_e l}{k \lambda_p} \frac{ds}{dT} \qquad 4.3.12$$

is the phase difference of the probe beam between the beam centre $r_1 = 0$ and $r_1 = 2^{1/2} \omega_e$,[40] where r_1 is the radial distance from the beam centre in the sample. P_e is the total power of the excitation laser, A_e the optical absorption coefficient of the sample at the wavelength of the excitation beam, K the thermal conductivity of the sample, λ_p the wavelength of the probe beam, $\frac{ds}{dT}$ ($s = nl$), is the temperature coefficient of the optical path length of the sample given as [41]

$$\frac{ds}{dT} = \frac{n-1}{l}\frac{dl}{dT} + \frac{dn}{dT}.$$

4.3.13

Here, n and l are the refractive index and thickness of the sample, respectively.

In liquid samples this coefficient is equal to the usual thermo-optical coefficient dn/dT. In

solid sample, ds/dT includes the influence of the thickness change due to temperature in

addition to dn/dT. If all the other parameters in Equation 4.3.12 are known for the

sample, either directly or by calibration using water, the phase-shift measurement yields

the absolute absorption coefficient, A_e.

4.3.3.2. Experimental

In figure 4.3.10 shows the experimental set-up of the pump-probe thermal lens

experiment. A continuous wave (*cw*) Titanium-Sapphire laser generates the pump field in

the spectral region 700 nm–980 nm with a peak power of 500 mW. The pump field

passes through a chopper C operating at low frequency (7 Hz). Using a prism P_1 and an

achromatic lens L_1 with a focal length of 20 cm, the pump beam on the sample is

focussed. The probe beam is a *cw* 1 mW Helium-Neon laser operating at 632nm. Using

the mirror M_2, the beam-splitter B_1 and lens L_2, the probe beam is focussed onto the

sample cell. By tilting the mirror M_2 and the beam-splitter B_1 the pump and the probe

beams are overlapped. After the propagation through the sample the probe beam is

directed towards the detector and the pump beam is blocked using three infrared filters

located at the detection plane. The probe beam passes through an interference filter with a
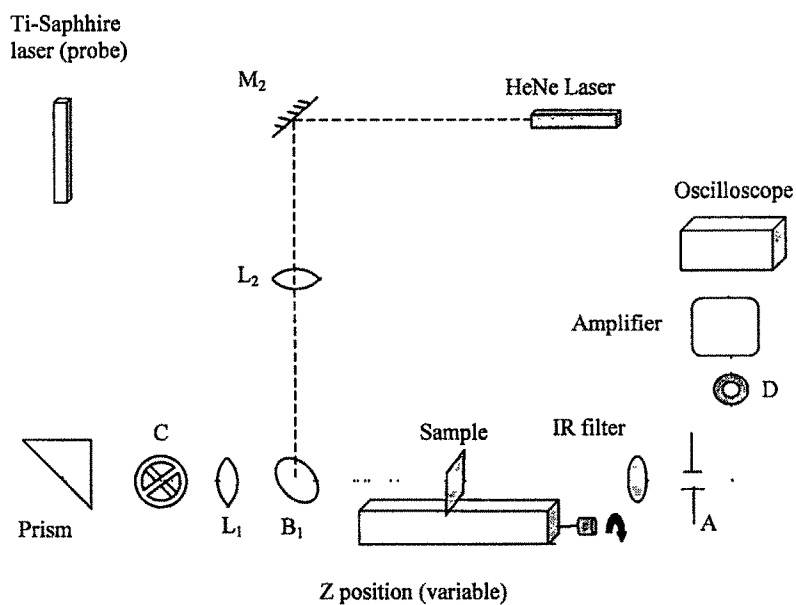
Figure **4.3.10** Experimental set-up consisting of a pump light source (cw Ti-Saphhire laser), a probe light source (632 nm, 1 mW He-Ne laser), chopper C, mirrors M_1 and M_2, lenses L_1 and L_2, beam-splitter B_1, sample-cell S, pump light filter F, Aperture A, detector D, a current amplifier and a digital oscilloscope.

high transmission at λ=632nm located at the detection plane. The probe beam has a $1/e^2$ diameter of 3 cm at the detector plane. An aperture with a diameter of 0.2 cm is placed in front of the detector. The signal from the detector is amplified for further processing. The ZTS crystal sample is orientated such that the pump and the probe beams propagate along the crystallographic [100] direction. Along this direction the sample has a length of 1 mm. A glass cell with a 1 mm path-length filled with distilled water is used for calibration. For the thermal lens spectroscopic experiment the sample is placed at the z position for which the observed signal is maximum. For the Z-scan experiment the sample is translated over a distance of about 6 cm about the focal point.

As seen from Equation 4.3.12, the extraction of the absolute absorption coefficient from the experiment requires the ds/dT coefficient, which is determined for ZTS using an interferometric method as shown in figure 4.3.11. In this method a laser beam at the required wavelength is split into two arms of a Mach-Zehnder interferometer. The two arms are recombined and expanded using a lens to observe an interference pattern with vertical fringes. A ZTS crystal with a known length, L, is placed on a temperature-controlled thermo-electric cooler (TEC) and introduced in one arm of the interferometer. The alignment is fine-tuned to restore the vertical fringe pattern. The crystal temperature is varied in steps of 5^0C and the resulting translation of the interference pattern is recorded in terms of the number of fringes, N, crossing a reference line on the screen. This measurement yields dN/dT, which is used to calculate ds/dT using
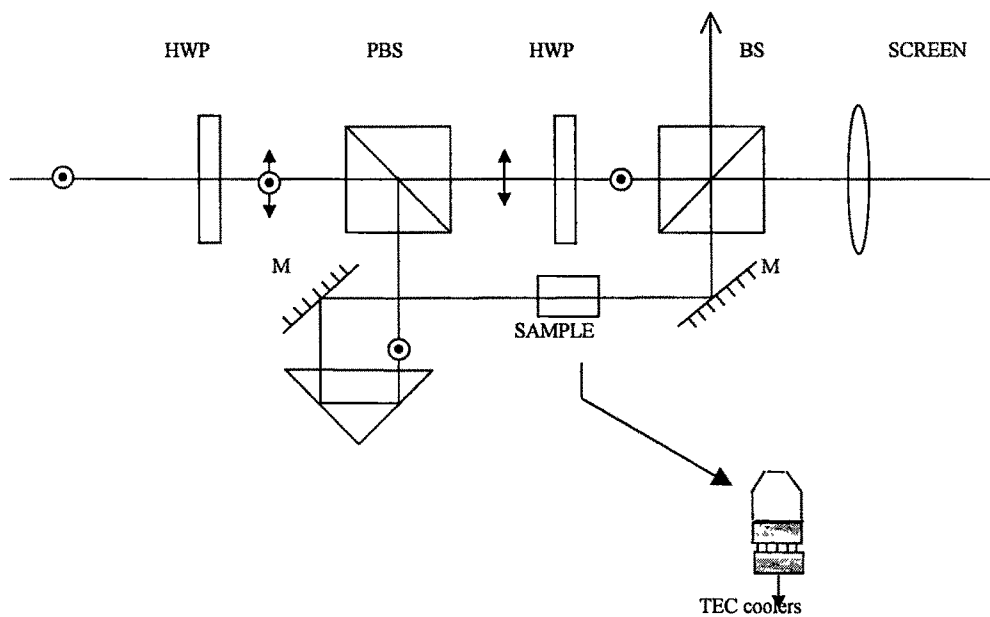
Figure 4.3.11. Interferometric method to measure the *ds/dT* for ZTS.

HWP   PBS   HWP   BS   SCREEN

M   M

SAMPLE

TEC coolers

$$\frac{ds}{dT} = -\frac{\lambda}{L}\left(\frac{dN}{dT}\right)$$

4.3.14

4.3.3.3. Results and discussion

. To calibrate our technique, a thermal lens spectroscopic experiment on distilled water is conducted by scanning the pump field in the region 700 nm-980 nm. In Fig. 4.3.12 the NIR spectrum of distilled water obtained using the thermal lens experiment and the one obtained using integrating cavity spectroscopy.[42, 43] Our results agree with the results of this transmission technique within an uncertainty of 5%. The close agreement between our result and the results in the cited references indicates good calibration of our experiment. The ZTS crystal is then placed at the same z-position and the thermal lens spectroscopic experiment is repeated. The result is shown in Fig. 4.3.13. The absolute values of the absorption coefficient can be estimated using the z-scan experiment described below.

Due to the possibility of the presence of higher order vibrational overtones, a careful characterization of the NIR spectrum of ZTS is necessary. ZTS has been known to have an absorption peak around 1040 nm, which has been attributed to an N-H vibrational overtone.[9] This absorption peak has been an impediment for the use of ZTS as a suitable frequency doubling crystal for the 1064 nm parent wavelength of the Nd:YAG laser. Attempts to shift the 1040 nm vibrational overtone to about 1400 nm by deuterating to yield d-ZTS crystals have not been satisfactory for two reasons: Deuterating leads to a lowering of the acceptance angle for SHG and does not allow noncritical phase
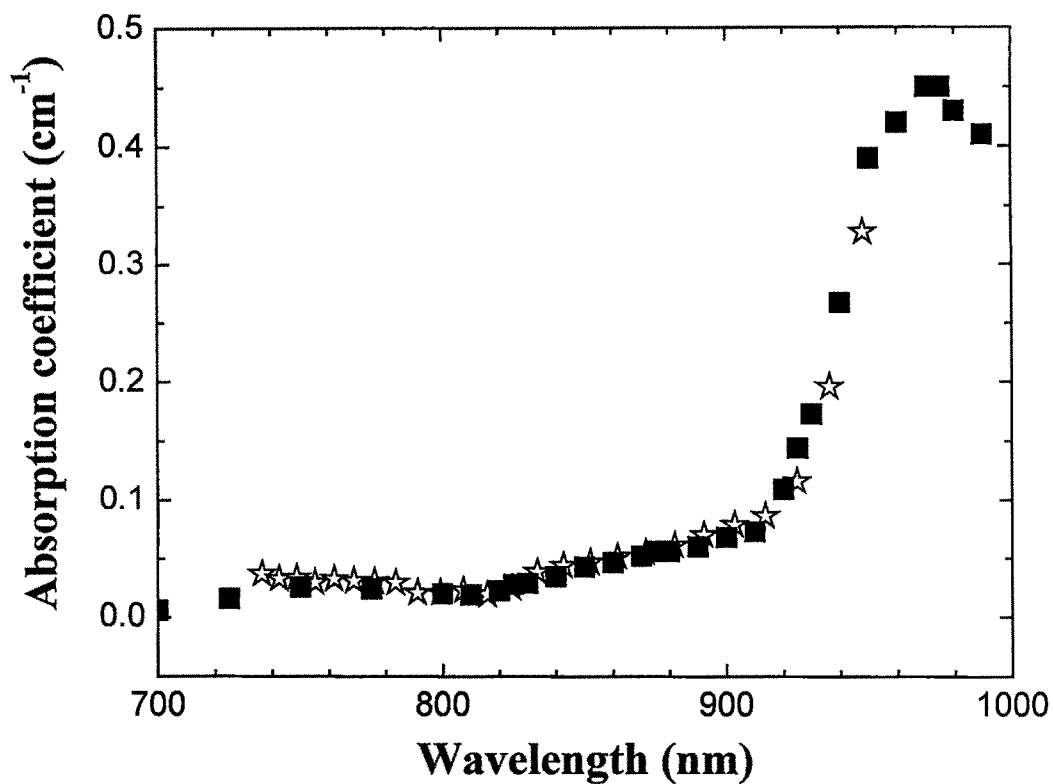
Figure 4.3.12 Thermal lens absorption spectrum of distilled water in the near infrared region (stars) measured with the set-up described in figure 4.3.10 . The squares are the measurements of absorption spectrum of water using transmittance methods.
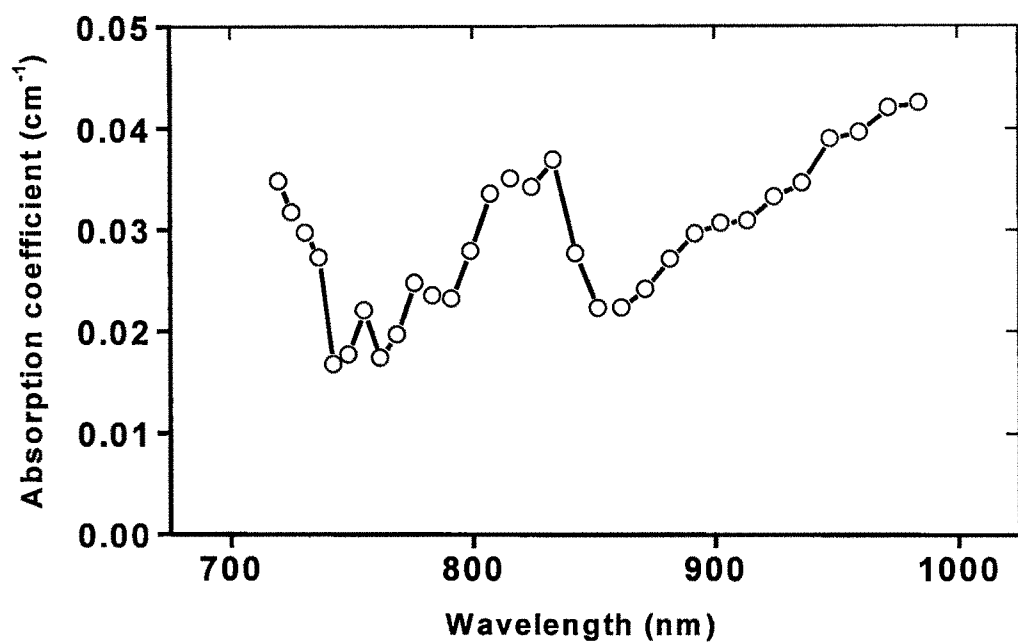
189

Figure 4.3.13 Thermal lens absorption spectrum of ZTS in the near infrared region measured under the same conditions of figure 4.3.10.

matching.[44] Due to the possibility of the presence of higher order vibrational overtones a careful characterization of the NIR spectrum of ZTS is necessary.

To measure the absolute values of the absorption coefficient of ZTS, thermal lens Z-scan experiment for the pump field wavelength of 920 nm and pump field power of 218 mW is performed. The results are plotted in figure 4.3.14. For calibration purposes the z-scan experiment of distilled water obtained under the same experimental conditions is plotted. The relative amplitude of the peak-valley Z-scan signal for water and ZTS, which gives the ratio of the phase shifts induced in these samples, is measured to be 0.87 ± 0.09. This gives the ratio of the phase-shifts induced in both samples. The absorption coefficient of ZTS can be calculated using equation 4.3.13 and the values of the experimental parameters for distilled water[45] and ZTS crystal[46] shown in Table 1. The thermal conductivity parameter, κ, for the ZTS crystal depends slightly on the crystal orientation as that is indicated in Table 1. For a laser beam propagating along the [100] direction in ZTS, the heat diffusion process involved in the formation of a thermal lens depends on both the transverse diffusion coefficients κ_2 and κ_3. For the sake of simplicity the average between these two values is used, as the Z-scan signatures do not change appreciably with the polarisation of the pump or the probe beams.
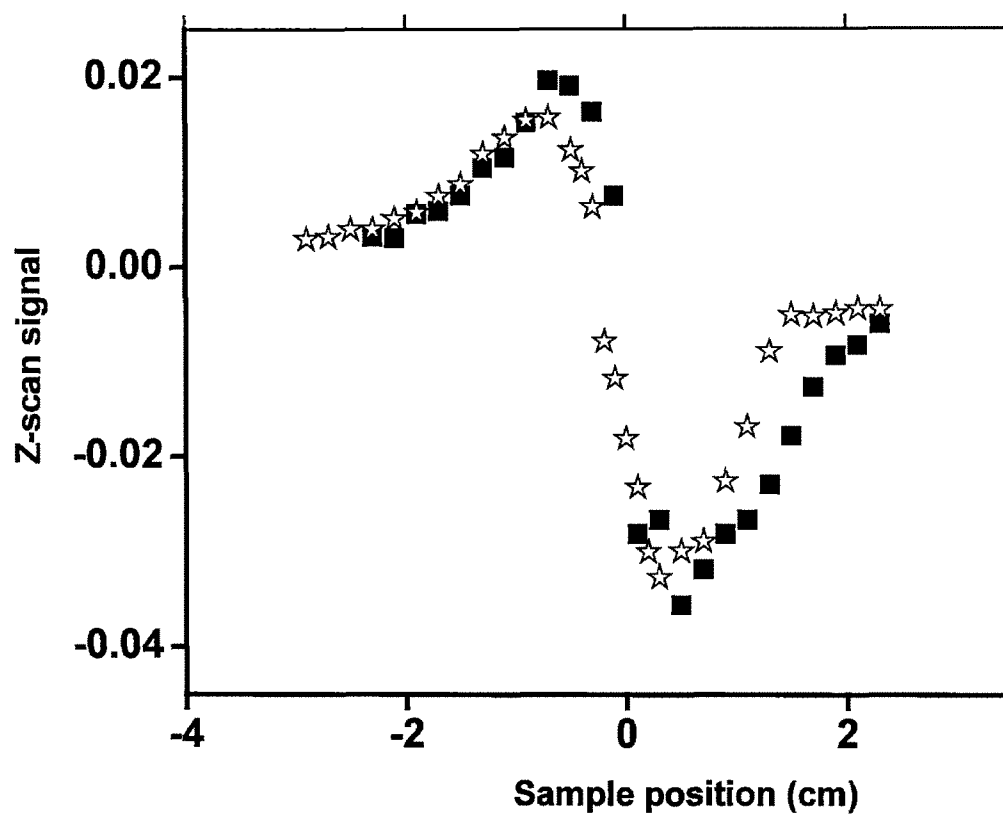
191

Figure 4.3.14. Z-Scan signal of distilled water (solid squares) and ZTS crystal (stars). The pump field power was 218W and the pump field wavelength was 920 nm.

Table 1 Photo-thermal paprameters of distilled water and ZTS crystal.

	n	L (cm)	$ds/dT \times 10^5$ (K^{-1})	κ (Wm^{-1}K^{-1})	α at λ=920 nm (cm^{-1})
H$_2$O	1.3	0.1	-9.1	0.598	0.12
ZTS	1.7	0.2	-9.3	κ_1= 0.34 κ_2= 0.54	0.03

Using Equation 4.3.12, for water we have,

$$\Phi_{H_2O} = \frac{P_e A_e l}{\lambda_{probe}} \left(\frac{ds}{dT} \right)$$

where $\lambda_{probe} = 632nm$, $\lambda_{pump} = 920nm$, $P_e = 218$ mW,

$$A_{H_2O}(920) = 0.12cm^{-1}$$

$$\frac{\Phi_{H_2O}}{\Phi_{ZTS}} = 0.87,$$

$$A_{ZTS} = \frac{\Phi_{H_2O}}{\Phi_{ZTS}} * A_{H_2O} * \frac{\left(\frac{ds}{dT}\right)_{H_2O}}{\left(\frac{ds}{dT}\right)_{ZTS}} * \frac{l_{H_2O}}{l_{ZTS}} * \frac{\kappa_{H_2O}}{\kappa_{ZTS}} = 0.033cm^{-1}$$

193

The Z-scan results show that the thermo-optical coefficient ds/dT is negative for both water and ZTS in agreement with the results of the measurements obtained using the interferometric method. Furthermore, the photo-thermal signal in Figure 4.3.15 confirms the negative sign of the nonlinearity. In Fig. 4.3.15, shows the thermal lens signal as a function of time for cell positions before and after the pump field focal point for both samples: water (a and b) and ZTS crystal (c and d). In each photo, the signal generated by chopping of the pump field is included. Before the focal point both samples give a signal in phase with the pump field (see Fig. 4.3.15, Frame a and c). After the focus, both materials give a signal 180° degree out of phase with respect the pumping field. Such behaviour is characteristic of a negative ds/dT. In ZTS, this means that the changes due to thermal expansion are smaller than the thermal changes of the refraction index, a situation that is not typical for solid state. The negative ds/dT has important consequences for the damage threshold of non-linear optical crystals. It contributes to the high damage threshold of ZTS by compensating for the self-focusing effects caused by Kerr nonlinearities. Our estimates of laser damage threshold in ZTS using a 1064 nm Nd:YAG, with 8 ns pulses at 10 Hz repetition rate, are of the order of 10 GW/cm^2 and will be published elsewhere. It is worth pointing that a negative ds/dT is observed in other well-known SHG crystals with high laser damage thresholds, such as LBO and BBO as that is shown in Table II Crystals with positive ds/dT and relative large absorption coefficients, like $AgGaS_2$ and $AgGaSe_2$, exhibit lower laser damage thresholds. KTP, which has a positive ds/dT, shows a higher damage threshold as its absorption coefficient is low. ZTS shows absorption peaks at 750 nm and at 850 nm with absorption coefficient of the order of 0.04 cm^{-1}. It is noted that although the absorption coefficient of ZTS is
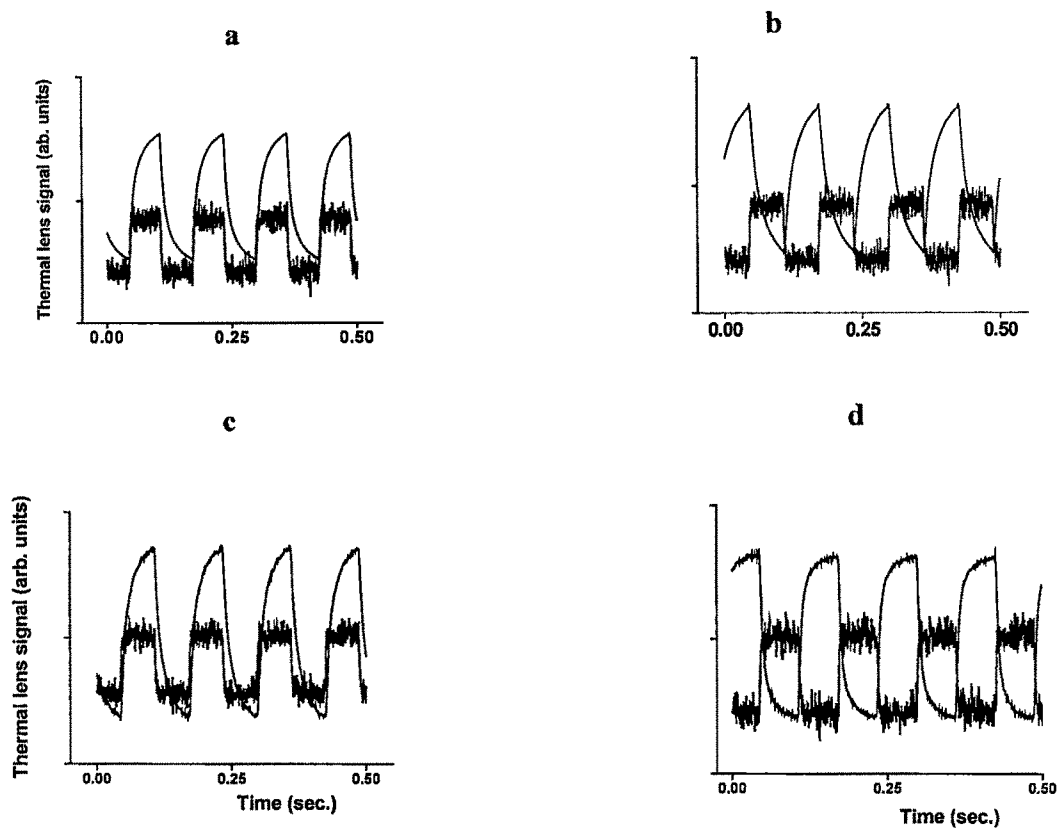
Figure 4.3.15. Thermal lens signal of distilled water (a and b) and ZTS crystal (b and d) measured when the sample cell was at 1 cm before the pump beam focal point (photographs a and c) and 1 cm after the focal point (photographs c and d)

larger than the absorption in other SHG crystals, its laser damage threshold is high. This is probably a result of the compensation of the self-focusing effect by the negative thermal lens, which is more effective for larger absorption and larger negative thermo-optical parameter, as is the case for ZTS. This result suggests that the role of a negative ds/dT and larger absorption coefficients needs to be evaluated as an important figure of merit for high laser damage threshold SHG crystals.

Table II. Laser damage threshold, photo-thermal parameter and the absorption coefficients of SHG crystals

Nonlinear crystal	Damage threshold (GW/cm^2)	ds/dT (10^5 °C^{-1})	α at 1064 nm (cm^{-1})
KTP	0.45	1.33	< 0.001
BBO	10	-1.29	< 0.001
LBO	18.9	-2.92	< 0.001
AgGaS$_2$	0.025	15.4	0.01
AgGaSe$_2$	0.020	15	0.05
ZTS	10	-9.3	0.03 at 920 nm

To understand the relationship between the pump field power and the absorption process, Z-Scan measurement for different powers of the pump beam was carried performed. Figure 4.3.16 shows the Z-scan signal of ZTS for different pump field powers: 217 mW (triangles), 125 mW (circles) and 57 mW (squares). The rest of the
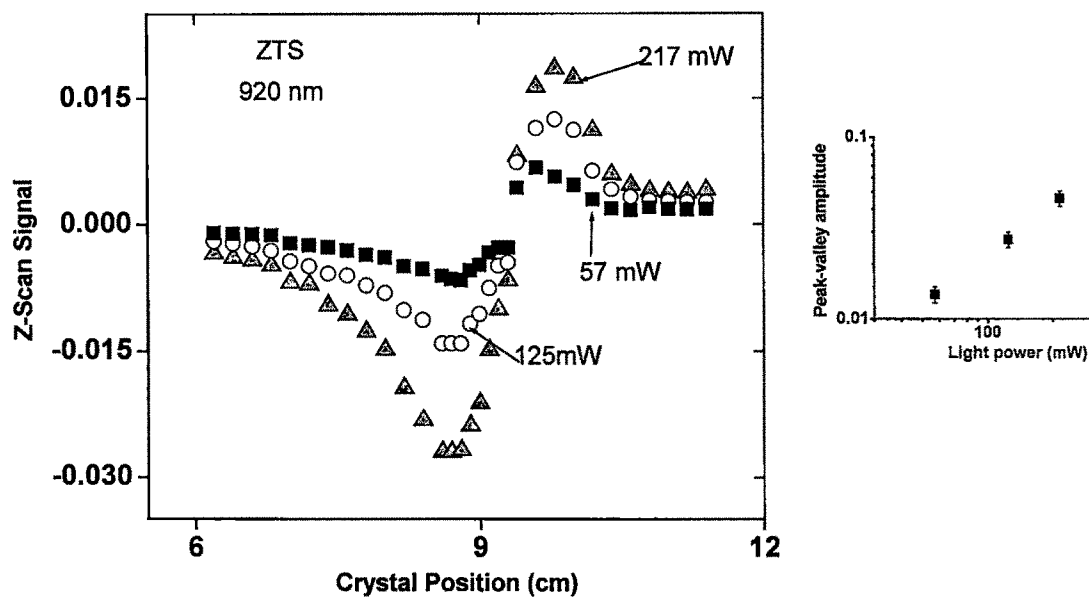
Figure 4.3.16. Z-Scan signal of the ZTS crystal at different pump field powers. The peak-valley amplitude pump power dependence is shown in the inset of the same figure

197

parameters are the same as in figure 4.3.14. In the inset of this figure, the valley peak amplitude of ZTS as a function of the pump field power is also plotted. The linear dependence corresponds to a one-photon absorption process.

4.3.4. Conclusion

The optical band gap of the ZTS crystal, obtained with IR spectra, was found to be 3.0 eV, in agreement with the earlier reported value. The absorption coefficient is minimum for crystals grown from solutions with pH in the range 3.5 to 3.8. This suggests that the crystals from pH 3.6 are of better quality and of more transparency. The variation of the absorption coefficient with solution pH closely follows the variation of the growth rate per unit mass with solution pH

This section of the thesis explains thermal lens and Z-scan measurement of the absorption coefficient for ZTS in the near-infrared region of the spectrum. This is particularly needed if a non-linear crystal is to be used for intra-cavity laser applications. In ZTS, the presence of the N-H vibrational overtone absorption at 1040 nm opens the possibility of higher order overtones being present in the near infrared spectral region. A careful characterization of NIR absorption of ZTS indicates an absorption coefficient of the order of 0.04 cm^{-1} at 820 nm. This absorption is very small and should not hinder the use of ZTS for nonlinear applications requiring high intensity laser inputs at NIR wavelengths. The Z-scan results show that the coefficient ds/dT is negative for both water and ZTS. The relatively high damage threshold of ZTS can be attributed to a compensation of the self-focusing effects caused by Kerr nonlinearities by the thermal lens resulting from a negative ds/dT. This study further demonstrates the suitability of

thermal lens and Z-scan techniques for measurement of small absorption and the thermo-optical parameters in nonlinear optical crystals.

.

REFERENCES

1. S. Selvasekarapandian, K. Vivekanandan, *et al*. Cryst. Res. Technol. **32**, 299 (1997).

2. V. Venkataramanan, C. K. Subramanian and H. L. Bhat, J. Appl. Phys. **77**, 6049 (1995).

3. V. Venkataramanan, M. R. Srinivasan and H. L. Bhat, J. Raman Spectrosc. **25**, 805 (1994).

4. Ben G. Streetman : *"Solid State Electronic devices"*, Prentic-Hall of Indian Pvt. New Delhi (1982).

5. S. M. Sze : *"Physics of Semiconductor devices"* : Wiley eastern limited New Delhi (1979).

6. R, Toar Barradas, C. Rincon, J. Genzalez and G. Sancher Pertez ., J. Phys. Chem. Solids **45**, 1185 (1984).

7. Eva C. Freeman and Willam Paul., Phys. Rev. B **20**, 716 (1979).

8. J. Mendolia and D. Lemone., Phys. State Sol. (a) **97**, 601 (1986).

9. H. O. Marcy, L. f. warren, L. E. Davis , M. S. Webb and S. P. Velsko, Mater. Optical info. Processing Symp. (Anaheim, CA, USA, 1-3 May 1991, Mater. Res. Soc., p.351, (1992).

10. P. M. Ushasree, R. Jayavel, Ramasamy, C. Subramanian, J. Cryst. Growth, **197**, p. 216-220,(1999)

11. Ushasree, P. M., Jayaval R., Ramasamy, Materials Chemistry and Physics, **61**(3), p. 270-274, Nov 1, 1999)

12. J. P. Gordon, R. C. C. Leite,R .S. Moore, S.P. S. Porto, J. R. Whinnerty : J. Appl. Phys. **36**, 3 (1965)

13. J. R. Whinnerty: Arc. Chem. Res. **7**, 225 (1974)

14. S. J. Sheldon, L. V. Knight, J. M. Throne: Appl. Opt. **21**, 1663 (1982)

15. D. A. Cremers, R. A. Keller : Appl. Opt. **21**, 1654 (1982)

16. J. Stone : Appl. Opt. **12**, 1828 (1973)

17. A. Hordvik: Appl. Opt. **16**, 2827 (1973)

18. Y. Othsuka, K. Itoh : Appl. Opt. **18**, 219 (1979)

19. A. C. Bocccara, D. Fournier, J. Bazod : Appl. Phys. Lett. **36**, 130 (1980)

20. P. E. Nordal, S. O. Kanstad : Phy. Scripta **20**, 659 (1979)

21. R. Santos, L. C. M. Miranda: J. Appl. Phys. **52**, 4194 (1981)

22. A. Rosencwaig : *"Optoacoustic Spectrocopy and Detection"*, ed. By Y. H. Pao

(Academic Press, Newyork 1977)

23. A. Hordvik: Appl. Opt. **16**, 2827 (1973)

24. N. J. Dovichi, J. M. Harris : Anal. Chem. **53** , (1981)

25. Dovichi, N. J. and Harris, J. M., Anal. Chem. **53**, 728 (1979)

26.]Dovichi, N. J. CRC Crit. Rev. Anal. Chem. **17**, 357 (1987)

27. Long M. E. , Swofford R. L., and Albrecht A. C., Science **191**, 183 (1976)

28. Sheik-Bahae M., Said A. A., Wei T. H., Hagan D. J. and Van Stryland E. W., IEEE J.

Quantum Electron. **26**, 760 (1990)

29. Castillo J., Kozich V. P. and A. Marcano O., Opt. Lett. **19**, 171 (1994)

30. Kozich V. P., A. Marcano O., Hernandez F. E. and Castillo J. A., Appl. Spec. **48**,

1506 (1994)

31 G. R. Long and S. E. Bialkowski, **56**, 2806-2811 (1984)

32. R. T. Bailey, F. R. Cruickshank, D. Pugh, A. McLeod, and W. Johnstone, Chem. Phys. **68**, 351 (1982)

33. N. J. Dovichi and J. M. Harris, Anal. Chem., **53**, 106 (1981)

34. S. Wu and N. J. Dovichi, J. Appl. Phys., **67**, 1170 (1990)

35. J. Shen, M. L. Baesso, and R. D. Snook, J. Appl. Phys., **75**, 3738 (1994)

36. T. Chen, S. J. Sheih, and R. D. Scott, Phys. Rev. B **43**, 615 , 385 (1991)

37. D. C. Johnson., Appl. Opt. **12**, 2192 (1973)

38. N. P Barnes, R. C. Eckhardt, D. J. Gettemy, and L. B. Edgett, IEEE J. Quantum Electron. **QE-15**, 1074 (1979)

39. T. C. Rich and Pinnow D. A., Appl. Phys. Lett, **20**, 264 (1972)

40. J. Shen,R.D. Lowe . and R. D. Snook, Chem. Phys. **165**. 385 (1992).

41. J. Shen, M. L. Baesso. and R. D. Snook, J. Appl. Phys. **75**, 3738 (1994).

42. Pope M. R., Fry E. S., Appl. Opt, **36**, 8710 (1997).

43. Query M. R., Gary P. G. and Waring R. C., Appl. Opt. **17**, 3587 (1978).

44. Ramabadran, U. B., McPherson, A. L. and Zelmon, D. E., J. Appl. Phys. **76**, 1150 (1994).

45. Stephen E. Bialkowski, *Photothermal Spectroscopy Methods For Chemical Analysis*, (John Wiley & Sons, New York, 1996)

46. P. Keroc, V. Venkataramanan, S. Lochran, R. T. Bailey, F. R. Cruickshank, D. Pugh, and J. N. Sherwood, J. Appl. Phys. **80**, 6666 (1996)